Hindawi
Journal of Chemistry
Volume 2022, Article ID 7270094, 23 pages
https://doi.org/10.1155/2022/7270094

Research Article

Structure-Based Virtual Screening, Docking, ADMET, Molecular Dynamics, and MM-PBSA Calculations for the Discovery of Potential Natural SARS-CoV-2 Helicase Inhibitors from the Traditional Chinese Medicine

Ahmed M. Metwaly,[1,2] **Alaa Elwan**,[3] **Abdul-Aziz M. M. El-Attar**,[4] **Sara T. Al-Rashood**,[5] **and Ibrahim H. Eissa**[3]

[1] *Pharmacognosy and Medicinal Plants Department, Faculty of Pharmacy (Boys), Al-Azhar University, Cairo 11884, Egypt*
[2] *Biopharmaceutical Products Research Department, Genetic Engineering and Biotechnology Research Institute, City of Scientific Research and Technological Applications (SRTA-City), Alexandria 21934, Egypt*
[3] *Pharmaceutical Medicinal Chemistry & Drug Design Department, Faculty of Pharmacy (Boys), Al-Azhar University, Cairo 11884, Egypt*
[4] *Pharmaceutical Analytical Chemistry Department, Faculty of Pharmacy, Al-Azhar University, Nasr City 11884, Cairo, Egypt*
[5] *Department of Pharmaceutical Chemistry, College of Pharmacy, King Saud University, P.O. Box 2457, Riyadh 11451, Saudi Arabia*

Correspondence should be addressed to Ahmed M. Metwaly; ametwaly@azhar.edu.eg and Ibrahim H. Eissa; ibrahimeissa@azhar.edu.eg

Received 6 March 2022; Revised 11 April 2022; Accepted 22 July 2022; Published 20 August 2022

Academic Editor: Ajaya Kumar Singh

Continuing our antecedent work against COVID-19, a set of 5956 compounds of traditional Chinese medicine have been virtually screened for their potential against SARS-CoV-2 helicase (PDB ID: 5RMM). Initially, a fingerprint study with **VXG**, the ligand of the target enzyme, disclosed the similarity of 187 compounds. Then, a molecular similarity study declared the most similar 40 compounds. Subsequently, molecular docking studies were carried out to examine the binding modes and energies. Then, the most appropriate 26 compounds were subjected to *in silico* ADMET and toxicity studies to select the most convenient inhibitors to be: (1*R*,2*S*)-ephedrine (**57**), (1*R*,2*S*)-norephedrine (**59**), 2-(4-(pyrrolidin-1-yl)phenyl)acetic acid (**84**), 1-phenylpropane-1,2-dione (**195**), 2-methoxycinnamic acid (**246**), 2-methoxybenzoic acid (**364**), (*R*)-2-((*R*)-5-oxopyrrolidin-3-yl)-2-phenylacetic acid (**405**), (*Z*)-6-(3-hydroxy-4-methoxystyryl)-4-methoxy-2*H*-pyran-2-one (**533**), 8-chloro-2-(2-phenylethyl)-5,6,7-trihydroxy-5,6,7,8-tetrahydrochromone (**637**), 3-((1*R*,2*S*)-2-(dimethylamino)-1-hydroxypropyl)phenol (**818**), (*R*)-2-ethyl-4-(1-hydroxy-2-(methylamino)ethyl)phenol (**5159**), and (*R*)-2-((1*S*,2*S*,5*S*)-2-benzyl-5-hydroxy-4-methylcyclohex-3-en-1-yl)propane-1,2-diol (**5168**). Among the selected 12 compounds, the metabolites, compound **533** showed the best docking scores. Interestingly, the MD simulation studies for compound **533**, the one with the highest docking score, over 100 ns showed its correct binding to SARS-CoV-2 helicase with low energy and optimum dynamics. Finally, MM-PBSA studies showed that **533** bonded favorably to SARS-CoV-2 helicase with a free energy value of −83 kJ/mol. Further, the free energy decomposition study determined the essential amino acid residues that contributed favorably to the binding process. The obtained results give a huge hope to find a cure for COVID-19 through further *in vitro* and *in vivo* studies for the selected compounds.

1. Introduction

The WHO disclosed on December 25, 2021 that the confirmed COVID-19 infections globally became over 276 million including more than 5 million dead persons [1]. These massive numbers demand enormous work from scientists all over the world to find a cure.

The utilization of natural products for the treatment has been mentioned since the oldest historical points [2]; the traditional medicines were unlimited sources for bioactive natural compounds such as flavonoids [3–5], alkaloids [6], saponins [7–9], isochromenes [10], α-pyrones [11, 12], diterpenoids [13], sesquiterpenoids [14, 15], and steroids [16].

Traditional Chinese medicine (TCM) is an ethnomedicine that authenticates the experience of ancient Chinese people in the treatment of different illnesses [17]. TCM is a reflection of a great experience of clinical practice that extended for thousands of years [18]. To date, the TCM remedies are still utilized effectively in China as well as several places of the world [19, 20].

Computer-aided drug design methodologies play an ever-increasing essential role in the discovery of new drugs [21, 22]. These methodologies have been very effective in the identification of new promising drug candidates with a noticeable limitation in time, cost, effort, and use of animal models [13–15]. The application of *in silico* methodologies included molecular docking [16–23], molecular design [24, 25], rational drug design [26–31], computational chemistry [32, 33], toxicity [34–36], ADMET [37–39], and DFT [40] assessments.

Our teamwork utilized computer-based methodologies to determine potential inhibitors against COVID-19 in various reports. For example, metabolites of *Artemisia sublessingiana* [41]þ and *Monanchora* species [42] were examined *in silico* against COVID-19. We suggested four isoflavonoids between a set of 59 as the most promising inhibitors against hACE2 and M^{pro} [43]. Recently, our team adjusted a multistep *in silico* filtration technique to select the most promising compound through a huge group of compounds against a certain COVID-19 protein. For instance, vidarabine was selected to be the most promising inhibitor against SARS-CoV-2 nsp10 [44]. Complementarily, the most convenient semisynthetic molecule against PLpro has been determined via a set of 69 compounds [45].

Helicases are pivotal enzymes in the viral lifecycle because of their responsibility to separate the dsDNA or RNA strands as well as their essential role in the process of RNA replication and repair [46]. Helicases can translocate molecules along the double-stranded (ds) DNA as well as RNA in a certain direction. Additionally, it can unwind (separate) the complementary strand of the DNA duplex through the dissociation of the hydrogen bonds between the nucleotide bases [47].

In this work, a collection of 5956 natural compounds, that were derived from traditional Chinese medicine and available at http://tcm.cmu.edu.tw/, has been subjected to structure and ligand-based *in silico* approaches (Figure 1) to determine the most convenient SARS-CoV-2 helicase inhibitors. The starting step in our research was (3*S*,4*R*)-1-acetyl-4-phenylpyrrolidine-3-carboxylic acid (**VXG**), the co-crystallized ligand of the SARS-CoV-2 helicase (PDB ID: 5RMM). **VXG** showed a high binding affinity against the target enzyme. Accordingly, it is expected according to the SAR principles that any compound with a similar structure could have a high binding affinity too. The utilized *in silico* methods included molecular structure similarity and fingerprint study against the **VXG**. Then, molecular docking against SARS-CoV-2 helicase (PDB ID: 5RMM) was conducted to examine the binding. ADMET and toxicity were utilized to make sure about the likeness of the selected compounds. Finally, molecular dynamics (MD) simulation experiments (RMSD, RMSF, R_g, SASA, and H-bonding) over 100 ns for the compound of the highest docking score, as well as MM-PBSA studies, were preceded to confirm the correct binding mode.

2. Results and Discussion

2.1. Molecular Filtration Using Fingerprint Method. The ligand-based *in silico* approach depends on the computation of chemical and physical properties of a molecule (ligand) and comparison of these properties with some biologically active compounds [48]. The fingerprint study is one of the ligand-based *in silico* methods that is vastly employed to predict the chemical structure's similarity or dissimilarity of two compounds or more [49, 50]. During the fingerprint study, the computer converts the chemical descriptors of a molecule to mathematical symbols. The obtained data are presented as bit strings. These strings describe the presence (1) or absence (0) of a certain 2D fragment or atomic descriptor (property) in the test and reference molecules [51, 52]. The co-crystallized ligand is a molecule that has a very high affinity to bind to a specific protein forming a ligand-protein complex in a crystallized form [53]. In consequence, the chemical structure of the co-crystallized ligand could be utilized effectively as a starting point to design and discover a potential inhibitor against the target protein.

Discovery studio 4.0 software was employed to examine the fingerprint similarity of 5956 natural compounds, which were derived from traditional Chinese medicine, against **VXG**, the co-crystallized ligand of SARS-CoV-2 helicase (PDB ID: 5RMM). The experiment determined 187 compounds to be the most similar candidates to **VXG** (Table 1). The study compared the following descriptors (properties) in the chemical structures of the experiment set and **VXG**: H-bond acceptor [54], H-bond donor [55], charge [56], hybridization [57], positive ionizable atoms [58], negative ionizable atoms [59], halogens [60], aromatic groups [61], and aligning with the $A\log P$ [62] of fragments as well as atoms.

2.2. Molecular Similarity. The difference between molecular similarity and fingerprint studies is that the fingerprint study computes the presence and/or absence of specific 2D atom

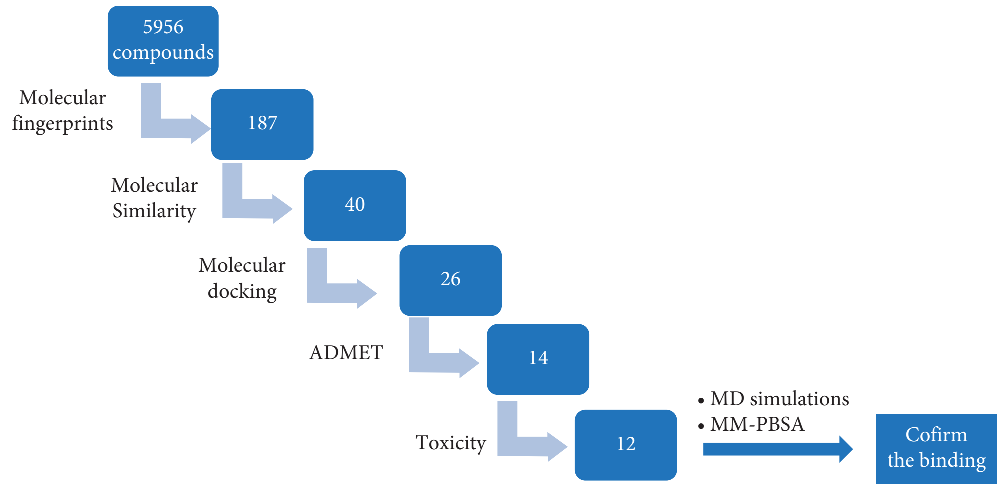

FIGURE 1: The employed computational techniques.

TABLE 1: Fingerprint similarity between 187 natural compounds and **VXG**.

Comp.	Similarity	SA	SB	SC	Comp.	Similarity	SA	SB	SC
VXG	1	166	0	0	**5412**	0.582205	602	580	−148
138	1	160	100	6	**1585**	0.581927	586	553	−132
167	1	169	118	−3	**1566**	0.581457	439	301	15
215	1	180	166	−14	**810**	0.581121	197	173	−31
258	1	153	128	13	**5449**	0.580863	431	288	23
347	1	143	101	23	**2379**	0.580247	329	113	125
364	1	90	−7	76	**5154**	0.579775	258	−9	196
379	1	143	101	23	**3239**	0.579154	589	563	−135
380	1	143	101	23	**2356**	0.57854	523	450	−69
411	1	112	42	54	**3258**	0.578205	451	326	3
445	1	186	146	−20	**3589**	0.578089	496	404	−42
496	1	196	201	−30	**362**	0.577495	272	17	182
501	1	163	145	3	**5439**	0.577398	608	599	−154
507	1	158	136	8	**3255**	0.577267	452	329	2
526	1	143	101	23	**1584**	0.576874	454	333	0
533	1	133	70	33	**71**	0.576792	169	127	−3
552	1	173	123	−7	**623**	0.576792	169	127	−3
554	1	173	121	−7	**38**	0.576087	265	6	189
555	1	173	121	−7	**5441**	0.576077	602	591	−148
577	1	154	90	12	**1982**	0.575087	494	405	−40
610	1	116	39	50	**398**	0.57485	96	1	70
619	1	156	131	10	**114**	0.561111	101	14	65
637	1	162	108	4	**816**	0.56	112	34	54
733	1	169	157	−3	**92**	0.556886	93	1	73
756	1	206	193	−40	**169**	0.556886	93	1	73
782	1	220	219	−54	**5157**	0.556701	108	28	58
792	1	207	178	−41	**451**	0.554878	182	162	−16
794	1	196	177	−30	**5154**	0.554307	148	101	18
803	1	169	147	−3	**768**	0.55418	179	157	−13
806	1	210	206	−44	**190**	0.553299	109	31	57
807	1	183	144	−17	**557**	0.55298	167	136	−1
818	1	99	9	67	**629**	0.55	176	154	−10
2379	1	213	229	−47	**495**	0.543333	163	134	3
405	0.777	136	9	30	**433**	0.538462	91	3	75
442	0.738	127	6	39	**754**	0.537764	178	165	−12
85	0.731	125	5	41	**566**	0.534743	177	165	−11
260	0.722	117	−4	49	**354**	0.534535	178	167	−12
208	0.697	124	12	42	**597**	0.53271	171	155	−5
91	0.689	122	11	44	**596**	0.531148	162	139	4

Table 1: Continued.

Comp.	Similarity	SA	SB	SC	Comp.	Similarity	SA	SB	SC
102	0.689	122	11	44	**601**	0.528302	168	152	−2
195	0.681	109	−6	57	**752**	0.527473	192	198	−26
280	0.674	116	6	50	**568**	0.526946	176	168	−10
344	0.658	121	18	45	**790**	0.526012	182	180	−16
370	0.658	121	18	45	**2368**	0.523041	227	268	−61
672	0.652	167	90	−1	**439**	0.522222	188	194	−22
48	0.649	113	8	53	**158**	0.521978	95	16	71
58	0.649	113	8	53	**5152**	0.521898	143	108	23
100	0.646	104	−5	62	**250**	0.520408	153	128	13
246	0.644	105	−3	61	**591**	0.519737	158	138	8
84	0.638	118	19	48	**5153**	0.517699	117	60	49
5169	0.636	159	84	7	**150**	0.517241	90	8	76
817	0.633	126	33	40	**297**	0.515789	147	119	19
396	0.624	106	4	60	**2370**	0.515738	213	247	−47
245	0.622	102	−2	64	**5167**	0.51567	181	185	−15
57	0.62	106	5	60	**413**	0.513986	147	120	19
65	0.62	106	5	60	**491**	0.513699	150	126	16
1942	0.614339	497	355	−43	**5177**	0.512195	189	203	−23
5415	0.614108	592	510	−138	**415**	0.511945	150	127	16
5434	0.614017	587	502	−133	**5151**	0.511696	175	176	−9
3941	0.613833	426	240	28	**2367**	0.511364	225	274	−59
4050	0.613551	489	343	−35	**544**	0.511299	181	188	−15
5441	0.613124	626	567	−172	**5159**	0.511111	92	14	74
5039	0.613119	458	293	−4	**266**	0.510903	164	155	2
4055	0.612984	491	347	−37	**374**	0.510563	145	118	21
3591	0.612751	519	393	−65	**418**	0.510417	147	122	19
2348	0.612622	563	465	−109	**5155**	0.510288	124	77	42
3912	0.612319	507	374	−53	**207**	0.510274	149	126	17
3579	0.612128	535	420	−81	**5149**	0.51005	203	232	−37
3919	0.611429	428	246	26	**5180**	0.508197	186	200	−20
5055	0.611111	440	266	14	**299**	0.507042	144	118	22
5168	0.61	158	93	8	**5158**	0.506329	120	71	46
539	0.609	162	100	4	**5176**	0.505208	194	218	−28
342	0.608	110	15	56	**397**	0.505051	150	131	16
511	0.608	178	127	−12	**614**	0.505017	151	133	15
784	0.607	193	152	−27	**622**	0.504983	152	135	14
564	0.605	182	135	−16	**512**	0.504615	164	159	2
201	0.604	186	142	−20	**5173**	0.50358	211	253	−45
542	0.589905	187	151	−21	**639**	0.503356	150	132	16
492	0.58885	169	121	−3	**50**	0.503165	159	150	7
228	0.586319	180	141	−14	**116**	0.502982	253	337	−87
2365	0.584081	521	438	−67	**80**	0.502092	120	73	46
3254	0.58408	587	551	−133	**3288**	0.502092	240	312	−74
206	0.583178	624	616	−170	**454**	0.502075	121	75	45
1571	0.582915	464	342	−10	**419**	0.501742	144	121	22
3591	0.582851	503	409	−49	**621**	0.50165	152	137	14
1593	0.582512	473	358	−19	**203**	0.501449	173	179	−7
59	0.582353	99	4	67	**3291**	0.501006	249	331	−83
64	0.582353	99	4	67	**86**	0.5	154	142	12
86	0.582278	276	20	178	**118**	0.5	100	34	66

SA, bits number in both similar natural compounds and **VXG**; **SB**, bits number in the similar natural compounds but not in **VXG**; **SC**, bits number in **VXG** but not in the similar natural compounds.

paths and descriptors regarding fragments or substructures in the examined compounds [63]. Contrastingly, the molecular similarity calculates specific molecular descriptors considering the whole chemical structure of compounds. These descriptors are steric, topological, electronic, and/or physical [64]. Utilizing Discovery studio 4.0 software, a molecular similarity study was done on the most similar 187 compounds against **VXG.** The applied descriptors in this study (Figure 2 and Table 2) were partition coefficient (*A*Log *p*) [65], molecular weight (M. W) [66], H-bond donors (HBA) [67], H-bond acceptors (HBD) [68], rotatable bond numbers [69], number of rings as well as aromatic rings [70], and minimum distance [71] together with the molecular

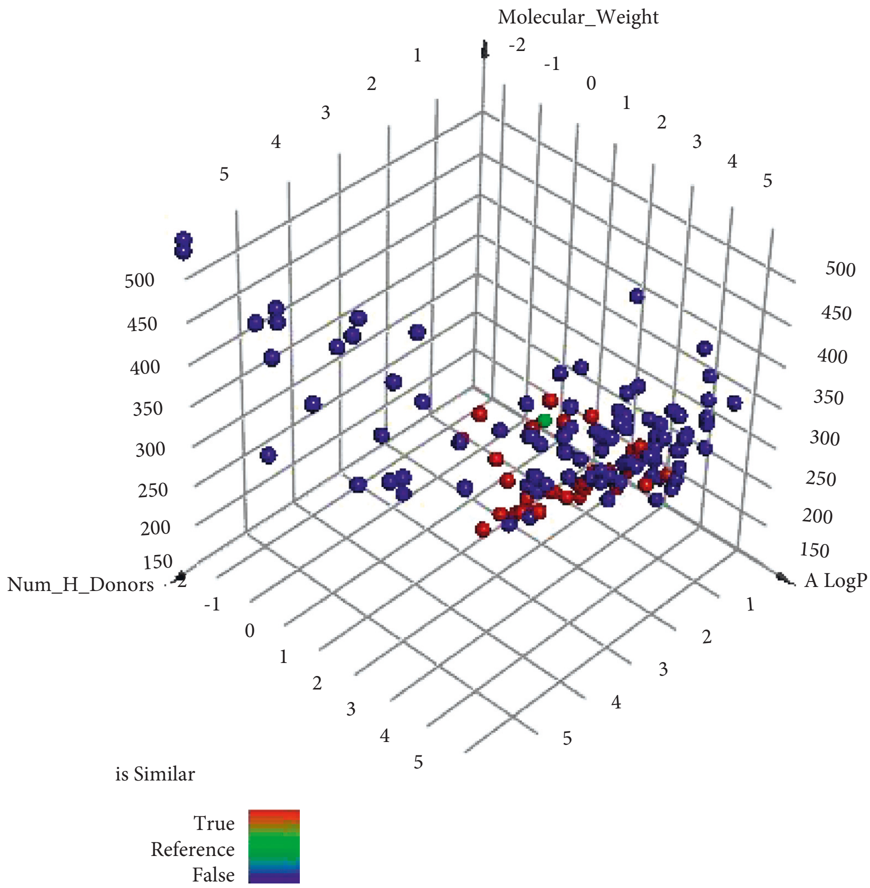

Figure 2: Molecular similarity of the examined compounds and **VXG**.

fractional polar surface area (MFPSA) [72]. The study was adapted to select the most similar 40 metabolites (Figure 3).

2.3. Docking Studies. Computer-aided drug design applies various techniques to optimize natural products into potentially active against certain biological targets [44, 45]. A molecular docking technique was applied for 40 **VXG** similar compounds against SARS-CoV-2 helicase (PDB ID: 5RMM). The binding modes and affinities of these compounds were examined.

The target protein was downloaded from Protein Data Bank (http://www.pdb.org), and Molecular Operating Environment (MOE .14) was used for the docking analysis. The docking process was validated by the re-docking of **VXG** inside the active pocket of the helicase protein. The root mean square deviation (RMSD) between the re-docked and the co-crystallized conformers was 0.74 A, which confirms the validity of the docking protocol (Figure 4).

Out of the examined 40 compounds, 26 displayed correct binding modes as well as good free energies. The promising compounds are as follows: (+)-methylpseudoephedrine (**48**), (1*R*,2*S*)-ephedrine (**57**), (1*R*,2*S*)-N-methylephedrine (**58**), (1*R*,2*S*)-norephedrine (**59**), (3*S*)-2,2-dimethyl-3,5-dihydroxy-8-hydroxymethyl-3,4-dihydro-2*H*,6*H*-benzo[1,2-*b*5,4-*b*′]dipyran-6-one (**80**), 2-(4-(pyrrolidin-1-yl)phenyl)acetic acid (**84**), (4*S*,5*R*)-ephedroxane (**85**), 1-phenylpropane-1,2-dione (**195**), 2-methoxycinnamaldehyde (**245**), 2-methoxycinnamic acid (**246**), 2-methoxybenzoic acid (**364**), 3′-*o*-acetylhamaudol (**374**), 3′-*o*-propionylhamaudol (**388**), (*R*)-2-((*R*)-5-oxopyrrolidin-3-yl)-2-phenylacetic acid (**405**), (*Z*)-6-(3-hydroxy-4-methoxystyryl)-4-methoxy-2*H*-pyran-2-one (**533**), 6,7-dihydroxy-2-(2-phenylethyl)-5,6,7,8-tetrahydrochromone (**539**), 7-demethylsuberosin (**610**), 8-chloro-2-(2-phenylethyl)-5,6,7-trihydroxy-5,6,7,8-tetrahydrochromone (**637**), 3-((*R*)-hydroxy ((*S*)-1-methylpiperidin-2-yl)methyl)phenol (**816**), (*R*)-((*S*)-1-methylpiperidin-2-yl)(phenyl)methanol (**817**), 3-((1*R*,2*S*)-2-(dimethylamino)-1-hydroxypropyl)phenol (**818**), (*R*)-4-(1-Hydroxy-2-(methylamino)ethyl)-7,7-dimethyl-5,6,7,8-tetrahydronaphthalen-1-ol (**5153**),(*R*)-4-(1-hydroxy-2-(methylamino)ethyl)-8,8-dimethyl-6,7,8,9-tetrahydro-5*H*-benzo [7]annulen-1-ol (**5155**), (*R*)-2-ethyl-4-(1-hydroxy-2-(methylamino)ethyl)phenol (**5159**), (*R*)-2-((1*S*,2*S*,5*S*)-2-benzyl-5-hydroxy-4-methylcyclohex-3-en-1-yl)propane-1,2-diol (**5168**), and (1*S*,4*R*,5*S*)-4-benzyl-5-(2-hydroxypropan-2-yl)-2-methylcyclohex-2-en-1-ol (**5169**).

The docking scores of the experienced ligands are predicted and summarized in Table 3. The binding modes of the

Table 2: Molecular descriptors of the examined 40 compounds and **VXG**.

Comp.	*A*Log *p*	M. Wt	HBA	HBD	Rotatable bonds	Rings	Aromatic rings	MFPSA	Minimum distance
VXG	0.71	233.26	3	1	2	2	1	0.237	
405	0.62	219.24	3	2	3	2	1	0.307	0.357
84	2.12	205.25	3	1	3	2	1	0.187	0.446
816	2.1	221.3	3	2	2	2	1	0.181	0.454
433	1.69	178.19	3	1	3	1	1	0.239	0.529
100	1.09	149.19	2	1	2	1	1	0.252	0.531
342	2.76	204.22	3	1	2	2	1	0.224	0.541
533	1.97	274.27	5	1	4	2	1	0.229	0.552
818	1.53	195.26	3	2	3	1	1	0.187	0.553
364	1.44	152.15	3	1	2	1	1	0.285	0.555
246	1.91	178.19	3	1	3	1	1	0.24	0.559
59	0.8	151.21	2	2	2	1	1	0.264	0.56
64	0.8	151.21	2	2	2	1	1	0.264	0.56
539	1.57	286.32	4	2	3	3	1	0.239	0.564
150	1.54	178.19	3	2	2	1	1	0.3	0.568
85	2.03	191.23	2	0	1	2	1	0.143	0.575
398	1.81	164.2	2	1	3	1	1	0.202	0.596
195	1.45	148.16	2	0	2	1	1	0.21	0.597
57	1.23	165.23	2	2	3	1	1	0.165	0.614
65	1.23	165.23	2	2	3	1	1	0.165	0.614
817	2.34	205.3	2	1	2	2	1	0.102	0.648
5168	2.17	276.37	3	3	4	2	1	0.198	0.672
5153	2.59	249.35	3	3	3	2	1	0.181	0.678
5159	1.56	195.26	3	3	4	1	1	0.231	0.691
118	2.22	203.28	2	0	0	2	1	0.122	0.695
374	2.4	317.36	4	2	2	3	1	0.244	0.706
245	1.93	162.19	2	0	3	1	1	0.143	0.713
48	1.77	179.26	2	1	3	1	1	0.105	0.715
58	1.77	179.26	2	1	3	1	1	0.105	0.715
114	2.2	194.23	3	0	4	1	1	0.157	0.731
610	3.51	230.26	3	1	2	2	1	0.192	0.738
388	2.01	333.36	5	2	3	3	1	0.264	0.743
5169	3.05	260.37	2	2	3	2	1	0.136	0.76
260	1.93	164.2	2	0	4	1	1	0.141	0.765
91	2.99	188.22	2	0	1	2	1	0.131	0.769
102	2.99	188.22	2	0	1	2	1	0.131	0.769
280	1.98	177.24	2	0	1	2	1	0.062	0.775
5155	3.04	263.38	3	3	3	2	1	0.171	0.782
637	1.37	336.77	5	3	3	3	1	0.282	0.784
208	2.16	191.27	2	0	1	2	1	0.057	0.795
80	0.9	292.28	6	3	1	3	1	0.337	0.81

tested ligands inside the active site of the target protein were depicted. The binding poses of the top five compounds with the highest energy scores as well as the most perfect modes were selected for detailed discussion as representative examples.

Starting with the binding interactions and orientation of the co-crystallized ligand (**VXG**) inside the active SARS-CoV-2 helicase (PDB ID: 5RMM), it revealed a binding affinity value of −19.37 kcal/mol. It showed a characteristic four hydrogen bonding interactions through carboxylate moiety of pyrrolidine ring with the essential amino acids SER486, ASN516, and ASN177. In addition, two hydrophobic interactions were formed between pyrrolidine ring and amino acid residues HIS554 and TYR515 (Figure 5).

The results of docking studies showed that the tested ligands have orientations and binding interactions similar to that of **VXG** against SARS-CoV-2 helicase. Three- and two-dimensional representations of binding modes of the most potent derivatives **533**, **637**, **84**, **195**, and **364** inside the active site of the target protein are depicted in Figures 6–10.

Compound **533** exhibited an interesting binding mode similar to that of the co-crystallized ligand against SARS-CoV-2 helicase with a docking score of −17.10 kcal/mol. It keeps the hydrogen bonding interactions with the essential amino acids SER486, ASN516, and ASN177. Also, it formed two additional hydrogen bonds with ASN179 and SER485 residues. Furthermore, compound **533** was incorporated in two hydrophobic interactions with amino acid residues HIS554 and TYR515 (Figure 6).

For compound **637**, the binding affinity was −18.85 kcal/mol. Such compound exhibited the best binding mode into

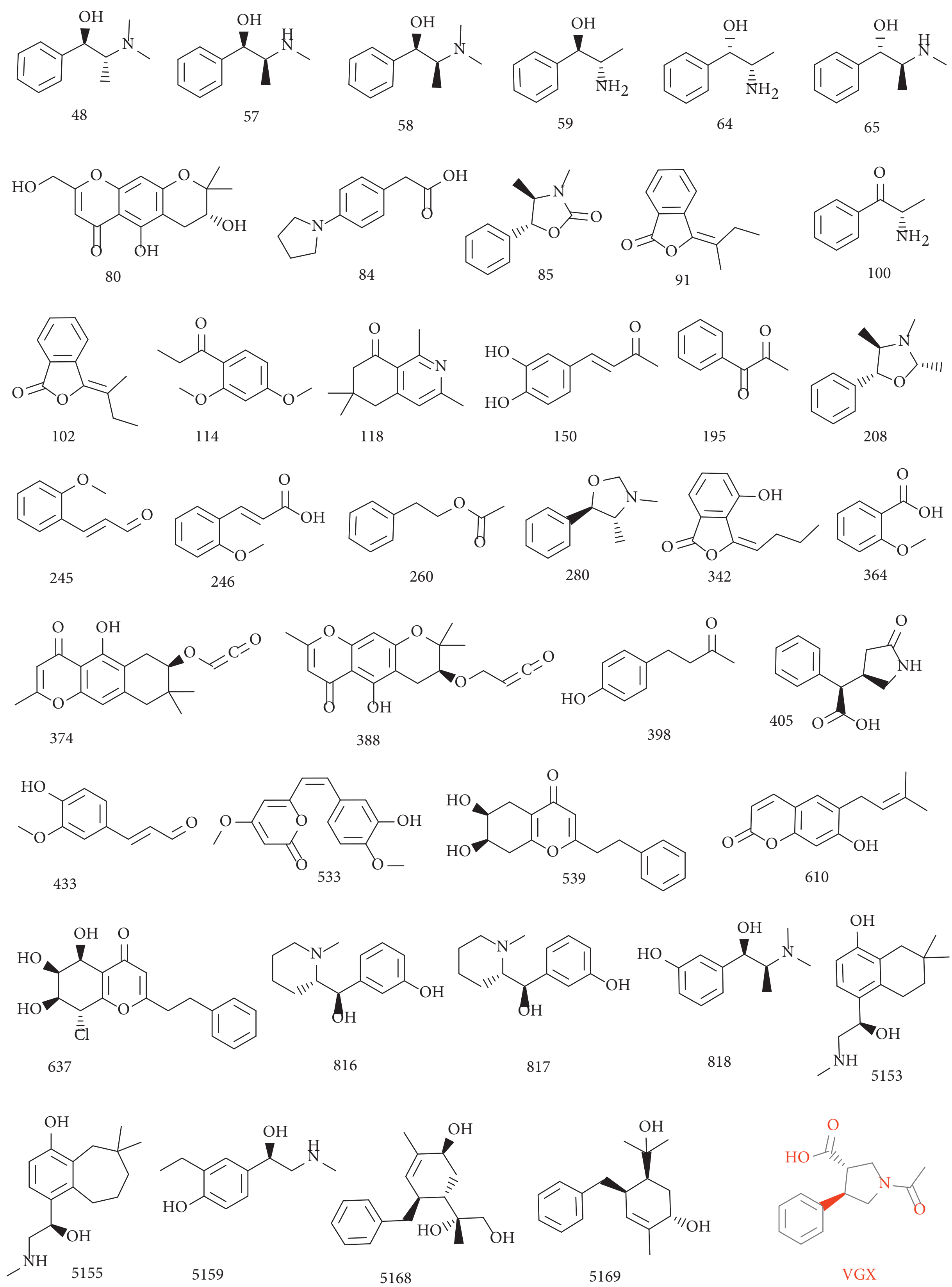

FIGURE 3: The most similar compounds to **VXG**.

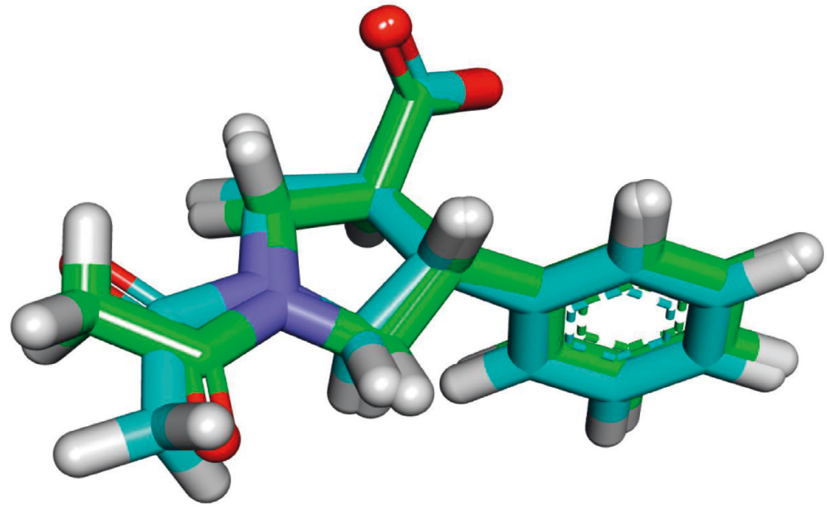

(a)

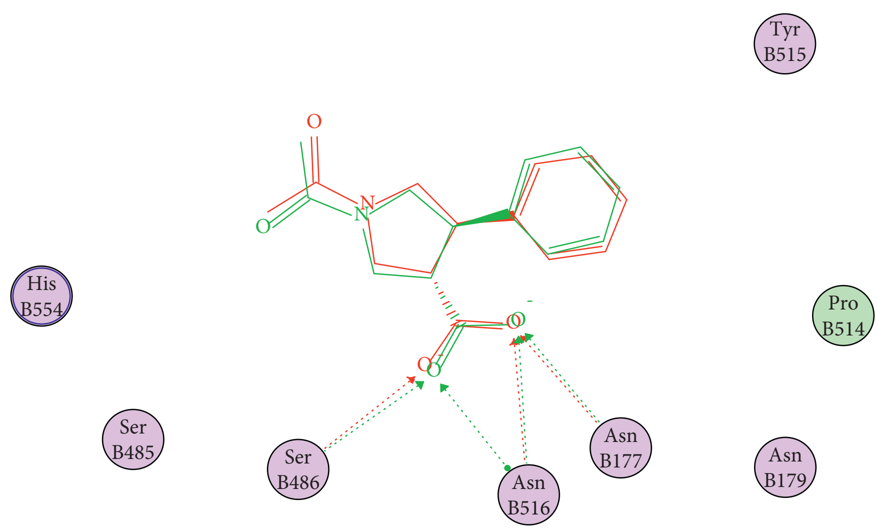

(b)

FIGURE 4: (a) 3D and (b) 2D superimposition of the re-docked conformer of **VXG** over the co-crystallized one with an RMSD value of 0.74 A.

TABLE 3: ΔG (in kcal/mole) of the most similar 40 compounds to **VXG**.

Compound	Name	ΔG (kcal/mole)
48	(+)-Methylpseudoephedrine	−15.92
57	(1*R*,2*S*)-Ephedrine	−15.64
58	(1*R*,2*S*)-*N*-methylephedrine	−15.24
59	(1*R*,2*S*)-Norephedrine	−14.29
64	(1*S*,2*S*)-Norpseudoephedrine	−13.65
65	(1*S*,2*S*)-Pseudoephedrine	−11.66
80	(3S)-2,2-Dimethyl-3,5-dihydroxy-8-hydroxymethyl-3,4-dihydro-2*H*,6*H*-benzo[1,2-*b*5,4-*b*′]dipyran-6-one	−14.27
84	2-(4-(Pyrrolidin-1-yl) phenyl) acetic acid	−15.46
85	(4*S*,5*R*)-Ephedroxane	−14.01
91	(*E*)-3-Butylidene phthalide	−13.31
100	(*S*)-Cathinone	−12.6
102	(*Z*)-3-Butylidene phthalide	−13.9
114	1-(2,4-Dimethoxyphenyl)-1-propanone	−13.53

Table 3: Continued.

Compound	Name	ΔG (kcal/mole)
118	1,3,6,6-Tetramethyl-6,7-dihydroisoquinolin-8(5*H*)-one	−12.41
150	(4*S*,5*R*)-Ephedroxane	−13.02
195	1-Phenylpropane-1,2-dione	−11.07
208	2,3,4-Trimethyl-5-phenyloxazolidine	−13.76
245	2-Methoxycinnamaldehyde	−14.92
246	2-Methoxycinnamic acid	−14.22
260	2-Phenylethyl acetate	−13.29
280	3,4-Dimethyl-5-phenyloxazolidine	−13.21
342	3-Butylidene-4-hydro-phthalide	−13.24
364	2-Methoxybenzoic acid	−12.16
374	3′-*o*-Acetylhamaudol	−18.21
388	3′-*o*-Propionylhamaudol	−18.13
398	4-(4-Hydroxyphenyl)-2-butanone	−12.88
405	(*R*)-2-((*R*)-5-Oxopyrrolidin-3-yl)-2-phenylacetic acid	−15.74
433	4-Hydroxy-3-methoxycinnamaldehyde	−13.11
533	(*Z*)-6-(3-Hydroxy-4-methoxystyryl)-4-methoxy-2*H*-pyran-2-one	−17.1
539	6,7-Dihydroxy-2-(2-phenylethyl)-5,6,7,8-tetrahydrochromone	−18.36
610	7-Demethylsuberosin	−15.48
637	8-Chloro-2-(2-phenylethyl)-5,6,7-trihydroxy-5,6,7,8-tetrahydrochromone	−18.85
816	3-((*R*)-Hydroxy ((*S*)-1-methylpiperidin-2-yl)methyl)phenol	−17.09
817	(*R*)-((*S*)-1-Methylpiperidin-2-yl) (phenyl)methanol	−15.95
818	3-((1*R*,2*S*)-2-(Dimethylamino)-1-hydroxypropyl)phenol	−15.79
5153	(*R*)-4-(1-Hydroxy-2-(methylamino)ethyl)-7,7-dimethyl-5,6,7,8-tetrahydronaphthalen-1-ol	−17.84
5155	(*R*)-4-(1-Hydroxy-2-(methylamino)ethyl)-8,8-dimethyl-6,7,8,9-tetrahydro-5*H*-benzo[7]annulen-1-ol	−16.59
5159	(*R*)-2-Ethyl-4-(1-hydroxy-2-(methylamino)ethyl)phenol	−17.89
5168	(*R*)-2-((1*S*,2*S*,5*S*)-2-Benzyl-5-hydroxy-4-methylcyclohex-3-en-1-yl)propane-1,2-diol	−18.4
5169	(1*S*,4*R*,5*S*)-4-Benzyl-5-(2-hydroxypropan-2-yl)-2-methylcyclohex-2-en-1-ol	−17.42
VXG	(3*S*,4*R*)-1-Acetyl-4-phenylpyrrolidine-3-carboxylic acid	−19.37

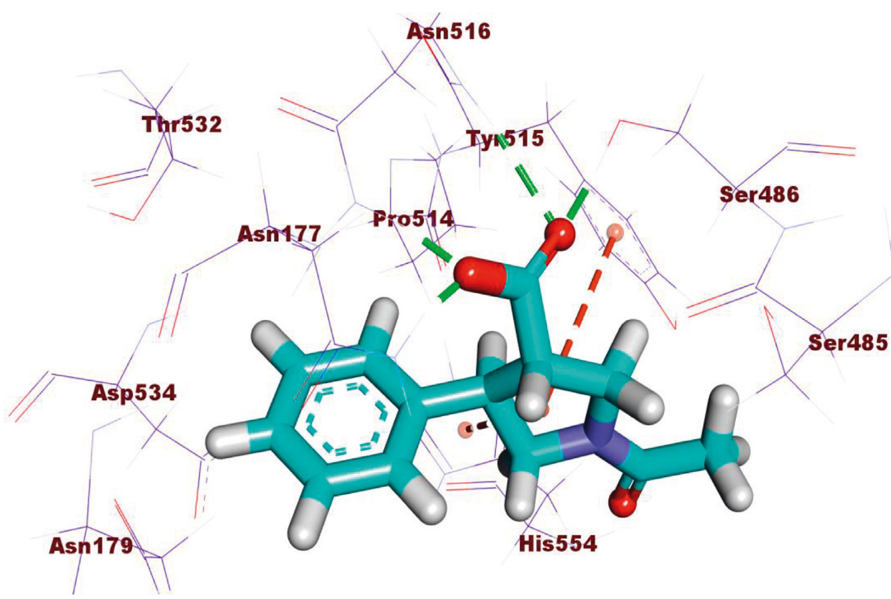

(a)

Figure 5: Continued.

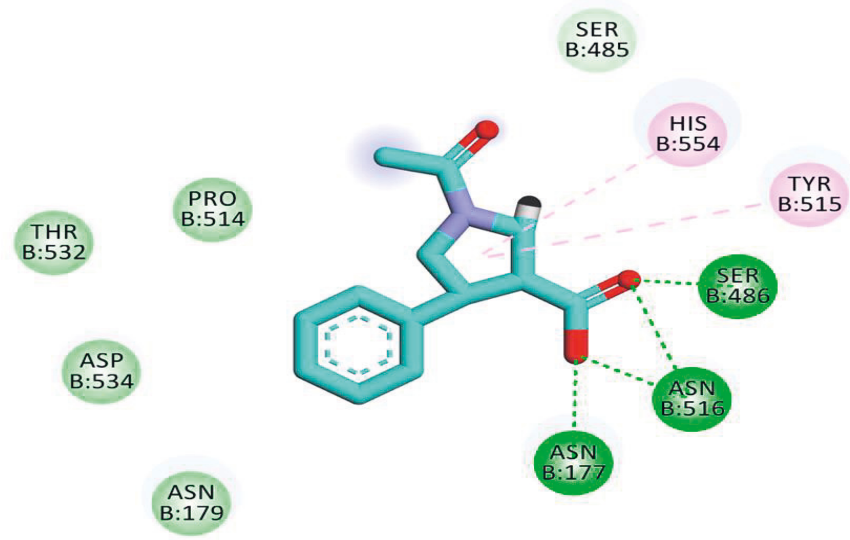

(b)

Figure 5: (a) 3D and (b) 2D of **VXG** docked into the active site of SARS-CoV-2 helicase.

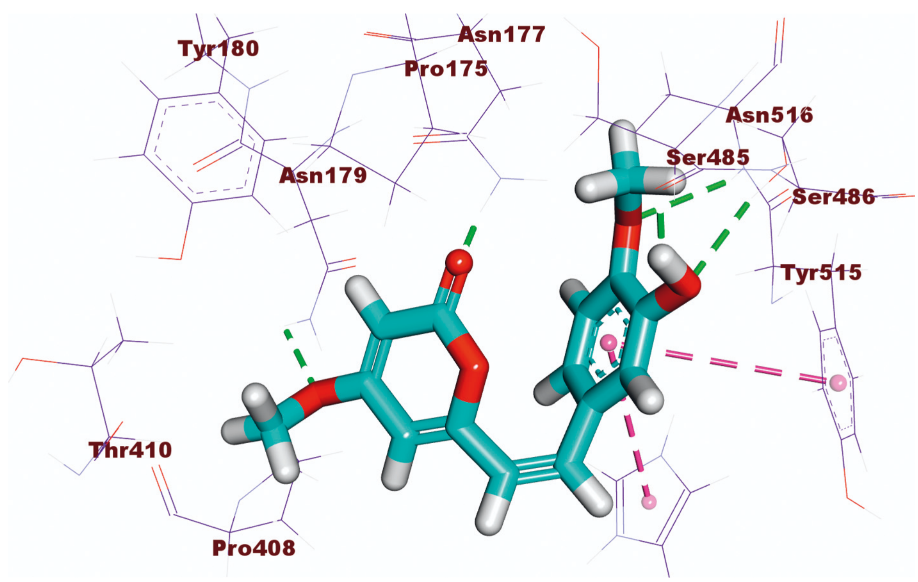

(a)

Figure 6: Continued.

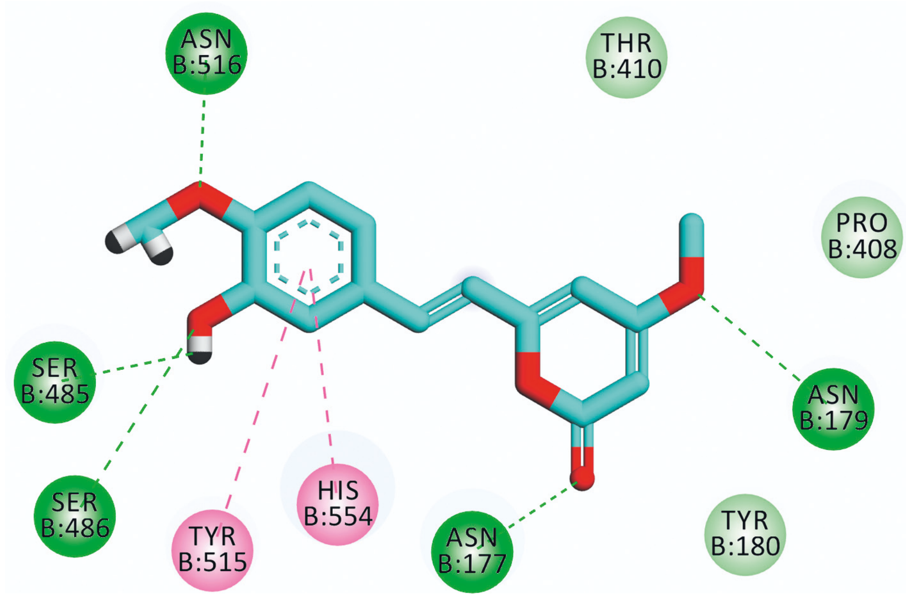

(b)

Figure 6: (a) 3D and (b) 2D images of the docked compound **533** into the active site of SARS-CoV-2 helicase.

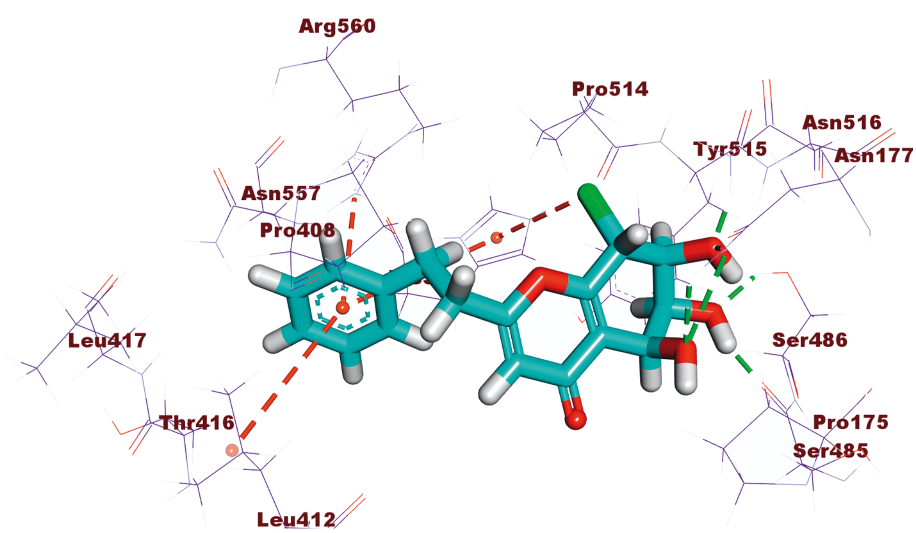

(a)

Figure 7: Continued.

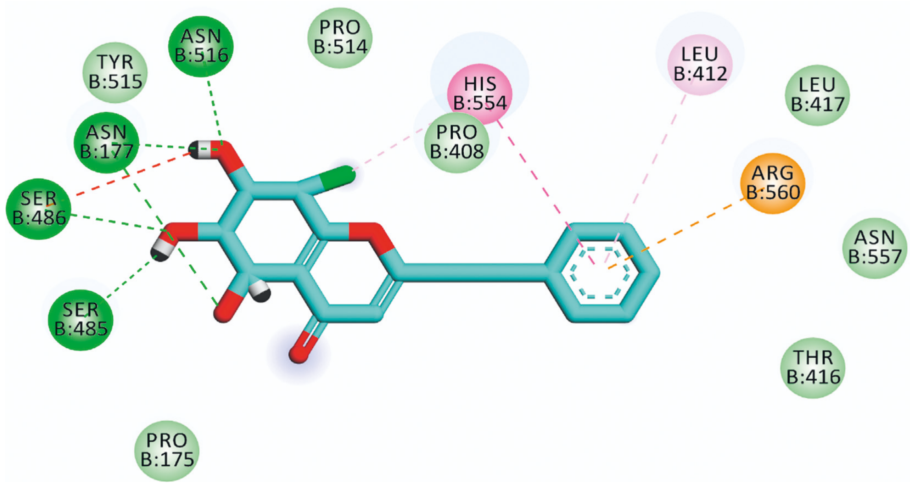

(b)

Figure 7: (a) 3D and (b) 2D images of the docked compound **637** into the active site of SARS-CoV-2 helicase.

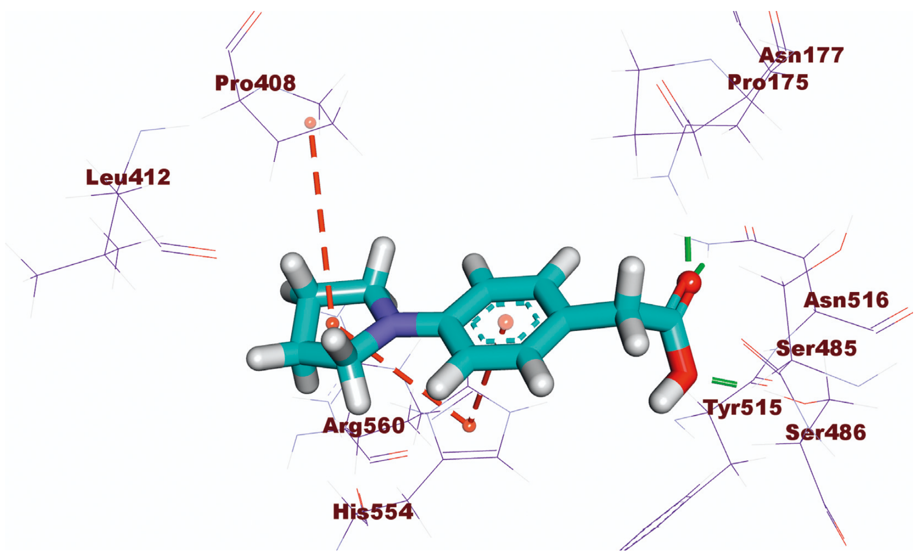

(a)

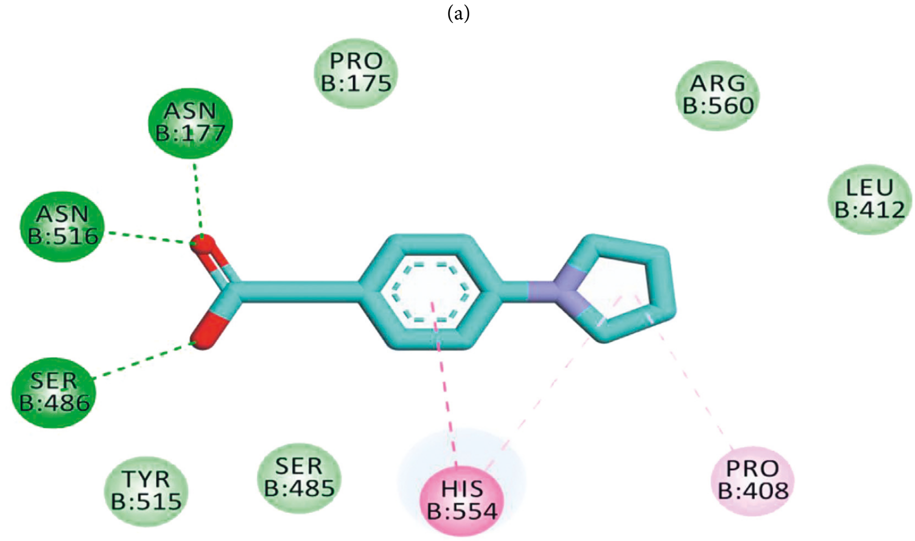

(b)

Figure 8: (a) 3D and (b) 2D images of the docked compound **84** into the active site of SARS-CoV-2 helicase.

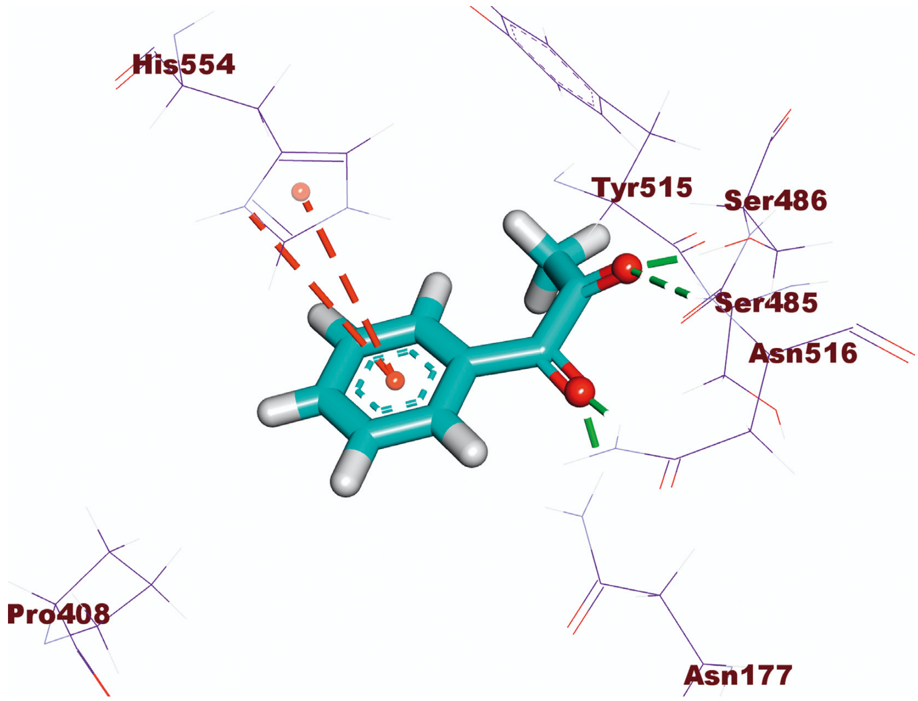

(a)

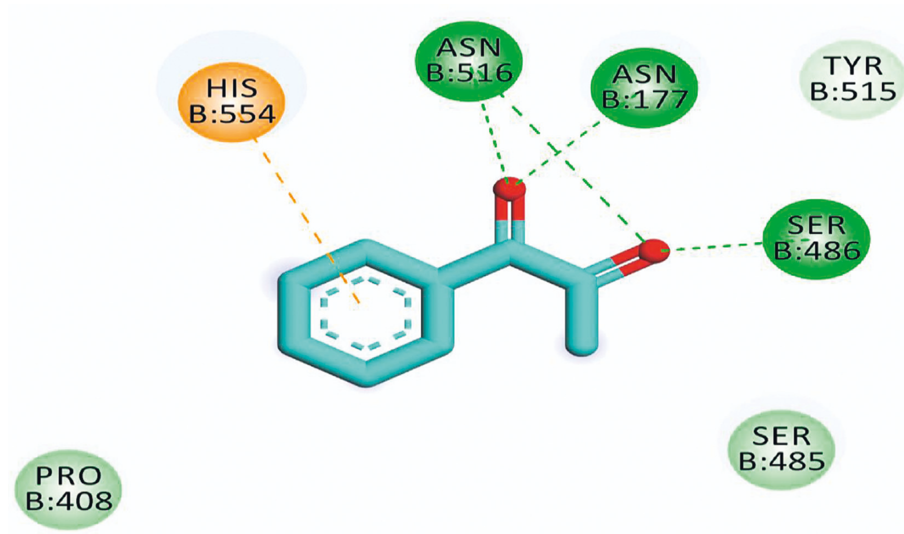

(b)

Figure 9: (a) 3D and (b) 2D images of the docked compound **195** into the active site of SARS-CoV-2 helicase.

the target protein, where it completely occupied the protein through seven hydrogen bonding interactions with SER486, ASN516, ASN177, SER485, and HIS554 residues. In addition, the terminal phenyl ring formed three hydrophobic interactions with HIS554, LEU412, and ARG560 residues (Figure 7).

Concerning the binding mode of compound **84** against SARS-CoV-2 helicase, the binding energy was −15.46 kcal/mol. The structural similarity of that compound with the co-crystallized ligand revealed the same binding mode against the receptor, where three hydrogen bonds were formed with SER486, ASN516, and ASN177 and three hydrophobic interactions were molded with HIS554 and PRO408 (Figure 8).

The binding affinity of compound **195** was −11.07 kcal/mol. Such affinity was represented by four hydrogen bonds with the key amino acids SER486, ASN516, and ASN177 and one hydrophobic interaction with HIS554 (Figure 9).

Finally, analyzing the binding interactions of compound **364** indicated a binding score of −12.16 kcal/mol. The carboxylate moiety formed three hydrogen bonding interactions with the key amino acids SER486, ASN516, and ASN177

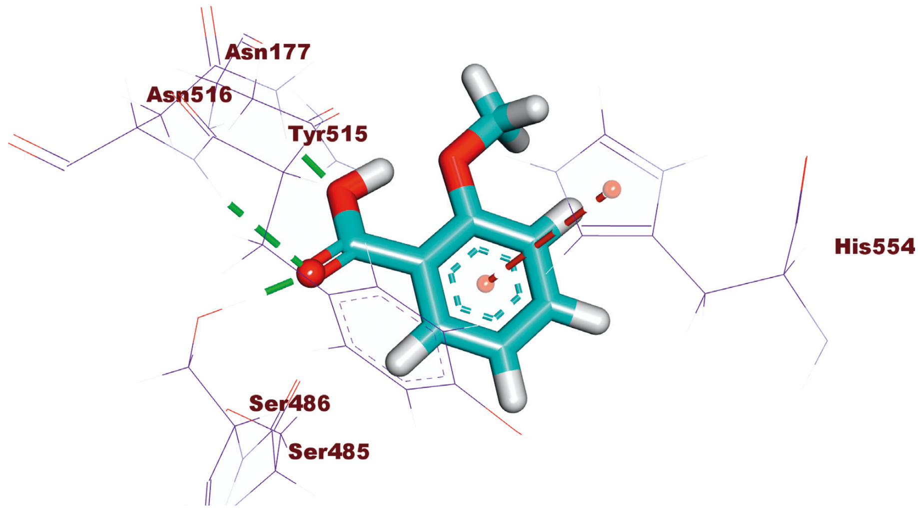

(a)

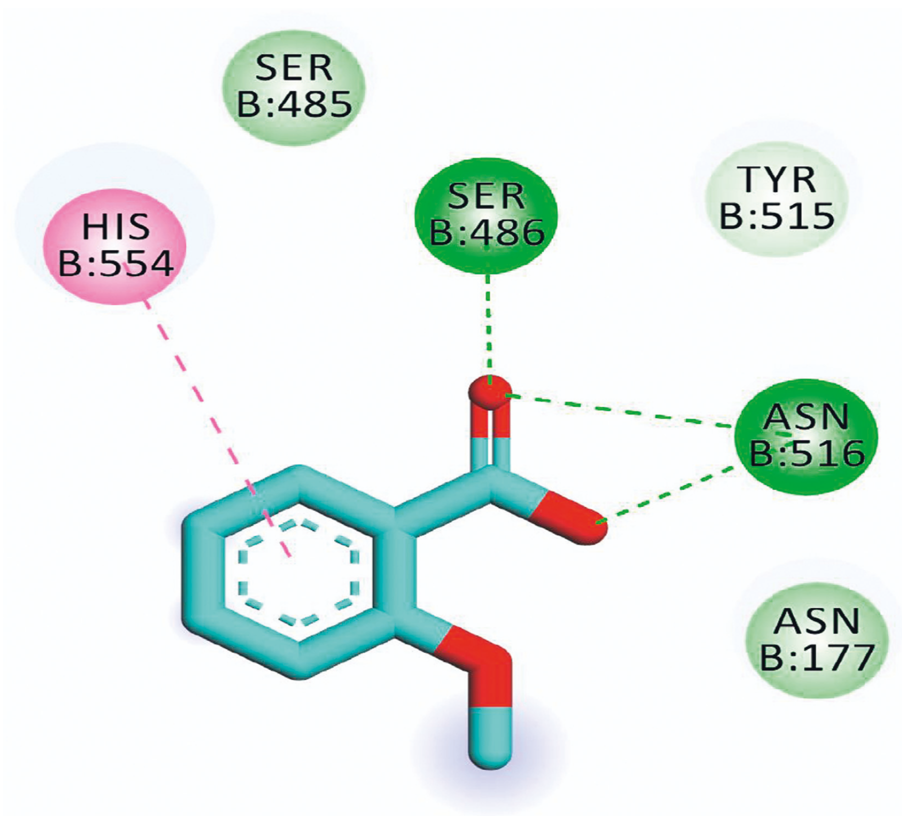

(b)

FIGURE 10: (a) 3D and (b) 2D images of docked compound **364** into the active site of SARS-CoV-2 helicase.

while the phenyl ring was incorporated in hydrophobic interaction with HIS55 (Figure 10).

2.4. ADMET Studies. The likeness of any molecule to be approved as a drug depends greatly on its pharmacokinetic properties as well as its activity. Subsequently, the investigation of the ADMET profile of a molecule should be considered in the early stages of drug design and discovery to avoid the withdrawal possibility of the drug from the pharmaceutical market [73]. These descriptors identify the absorption, distribution, metabolism, excretion, as well as the toxicity of the examined compound. Although, there are different *in vitro* experiments that can determine the ADMET profile, *in silico* determination is an available and reliable tool with the profit of being faster, cheaper, as well as and lifesaver of the experimental animals [74].

Table 4: ADMET profile of the 26 compounds with the best docking scores.

Comp.	BBB level[a]	HIA[b]	Aq[c]	CYP2D6[d]	PPB[e]
48	1	0	4	T	F
57	2	0	4	F	F
58	1	0	4	T	F
59	3	0	4	F	F
80	3	0	3	F	F
84	2	0	3	F	T
85	1	0	3	F	F
195	2	0	3	F	T
245	1	0	3	F	T
246	2	0	3	F	T
364	2	0	4	F	T
374	2	0	3	F	F
388	3	0	3	F	F
405	3	0	4	F	F
533	3	0	3	F	T
539	3	0	3	F	T
610	1	0	3	F	T
637	3	0	3	F	T
816	2	0	3	T	F
817	1	0	3	T	F
818	2	0	4	F	F
5153	2	0	3	T	T
5155	2	0	3	T	T
5159	3	0	4	F	F
5168	2	0	4	F	T
5169	1	0	3	F	T
Simeprevir	4	3	2	F	T

[a]BBB, ability to pass the blood-brain barrier, 1 is high, 2 is medium, 3 is low, and 4 is very low; [b]HIA, human intestinal absorption level, 0 is good, 1 is moderate, 2 is poor, and 3 is very poor; [c]Aq, aqueous solubility level, 0 is extremely low, 1 is very low, 2 is low, 3 is good, and 4 is optimal; [d]CYP2D6, inhibition of CYP2D6 enzyme, T is an inhibitor and F is a noninhibitor; [e]PPB, F means less than 90% and T means more than 90%.

The predicted ADMET profiles of the 26 compounds that showed correct modes of binding besides Remdesivir, the reference drug, are shown in Table 4 and Figure 11. Compounds **48**, **58**, **85**, **245**, **610**, **816**, **817**, **5153**, **5155**, and **5169** were excluded because of their predicted strong ability to pass the blood-brain barriers which may be combined with a CNS toxicity. Among the excluded compounds, compounds **48**, **58**, **816**, **817**, **5153**, and **5155** were predicted to be inhibitors against the CYP2D6 enzyme which would cause hepatotoxicity. The predicted intestinal absorption and aqueous solubility of all compounds were good to optimal.

2.5. Toxicity Studies. The early prediction of toxicity is a crucial step that minimizes drug failure because of toxicity in the development stage or the clinical trials [75]. *In silico* prediction of toxicity is a credible approach that plays an essential role in drug design and discovery of lead compounds because *in vitro* and *in vivo* approaches are usually controlled by strict ethical regulations, time, and availability of resources [76], whereas the *in silico* prediction is based on a structure-activity relationship toxicology. The software compares the essential structural descriptors of the examined compounds with a huge library of hundreds of thousands of reported safe and toxic compounds [77] (Supporting data (available here)). Discovery studio 4.0 software was employed to predict the toxicity profile of the selected compounds after the ADMET study against 7 models. The applied models are FDA rat carcinogenicity [78, 79], mouse carcinogenic potency (TD_{50}) [80], rat maximum tolerated dose (MTD) [81, 82], rat oral LD_{50} [83], rat chronic LOAEL [84, 85], ocular irritancy, and skin irritancy [86]. According to the obtained results (Table 5), compounds **80**, **388**, and **539** were eliminated due to the predicted high carcinogenic potency.

2.6. Molecular Dynamics (MD) Simulations. Despite the ability of molecular docking studies to expect the mode of binding of a compound inside a specific protein correctly, it has a serious defect that it deals with the protein as a rigid unit. Resultantly, it does not compute the conformational changes that happen in the protein because of ligand binding [87]. On the contrary, the MD simulations can adequately describe the behavior of a protein at the atomic level in full detail and at very accurate temporal resolution [88]. In accordance, the MD simulations have the advantage of being able to predict the conformational changes that occurred in the protein after ligand binding [89]. Furthermore, MD simulation studies can effectively compute various factors related to the energy of the protein-ligand complex for a determined time. Subsequently, it accurately describes the binding mode, stability, and flexibility of the ligand inside the target protein [90].

The first successful MD simulation experiment of a protein (bovine pancreatic trypsin inhibitor) was published in Nature in 1977 [91]. Fortunately, because of the recently introduced supercomputer hardware, especially the advanced graphics processing units, MD simulation experiments became much more accessible, powerful, and accurate [92].

In the MD simulation study, the forces on every atom of the examined ligand-protein complex are computed at every ultra-short time interval according to the basics of the "force field" [93]. The computed force field can be utilized to describe the position and velocity of atoms at each time interval. The force field is a physical expression that describes the functional potential energy of atoms. The force field is calculated based on Newton's laws of motion considering bonded interactions (bonds, angles, and dihedrals) in addition to nonbonded interactions (van der Waals potentials and Coulomb potentials) between all atoms of the complex. This step is repeated billions of times to produce the atomic trajectories for a specific time interval [94].

Several MD simulation studies were employed to investigate the stability and mimic the dynamic of compound **533**, (*Z*)-6-(3-hydroxy-4-methoxystyryl)-4-methoxy-2*H*-pyran-2-one, that exhibited the best docking score inside SARS-CoV-2 helicase for 100 ns.

First, the interaction of a ligand inside the active site of a protein leads to some changes in the structure of that protein [95]. In consequence, the dynamics and the conformational

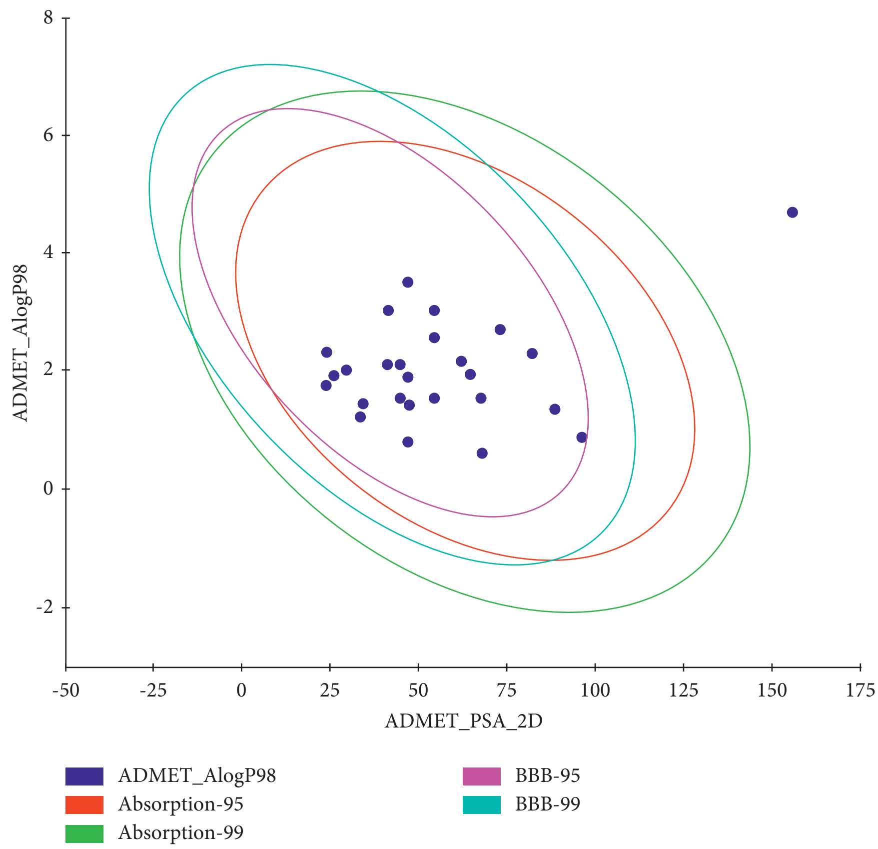

Figure 11: Results of the ADMET study.

Table 5: *In silico* toxicity profile of 15 compounds with good ADMET profile.

Comp.	FDA rat carcinogenicity (mouse-female)	TD_{50} ($mg \cdot kg^{-1} \cdot day^{-1}$)	MTD ($g \cdot kg^{-1}$)	Rat oral LD_{50} ($g \cdot kg^{-1}$)	LOAEL ($g \cdot kg^{-1}$)	Ocular irritancy	Skin irritancy
Simeprevir	Not a carcinogen	2.0138	0.002967	0.208835	0.0021057	Mild	None
57	Not a carcinogen	306.685	0.126925	0.678557	0.1091	Severe	None
59	Not a carcinogen	209.013	0.130669	1.17822	0.153373	Severe	None
80	Multicarcinogen	30.9654	0.320563	0.112645	0.0104398	Moderate	None
84	Not a carcinogen	86.2745	0.432043	0.651537	0.0466934	Severe	None
195	Not a carcinogen	734.376	0.0920234	0.80394	0.58711	Mild	None
246	Not a carcinogen	896.437	0.185908	0.975783	0.0690491	Mild	Mild
364	Not a carcinogen	1,152.33	0.178125	1.10017	0.269177	Mild	None
388	Multicarcinogen	77.4401	0.158212	0.128576	0.0111578	Severe	Mild
405	Not a carcinogen	1,019.87	0.355843	0.565566	0.0958513	Moderate	None
533	Not a carcinogen	587.516	0.109002	0.765306	0.026065	Mild	Mild
539	Multicarcinogen	71.1582	0.12354	0.366215	0.0229232	Severe	None
637	Not a carcinogen	30.3365	0.136595	0.428434	0.0201137	Severe	Mild
818	Not a carcinogen	145.39	0.355736	0.71245	0.0937066	Severe	None
5159	Not a carcinogen	227.599	0.559977	0.526787	0.0808567	Severe	None
5168	Not a carcinogen	128.911	0.242854	2.09646	0.0494677	Moderate	Mild

changes of the SARS-CoV-2 helicase-**533** complex were computed as root mean square deviation (RMSD) to detect the stability due to binding. It is observed that the SARS-CoV-2 helicase and **533** exhibited lower RMSD with no major fluctuations indicating their greater stability (Figure 12(a)). Interestingly, the SARS-CoV-2 helicase-**533** complex was stable till 90 ns~. Although the SARS-CoV-2 helicase-**533** complex showed a minor fluctuation later, it reached equilibrium again.

Second, the flexibility of SARS-CoV-2 helicase was calculated in terms of root mean square fluctuation (RMSF) to calculate the differences in flexibility in the SARS-CoV-2

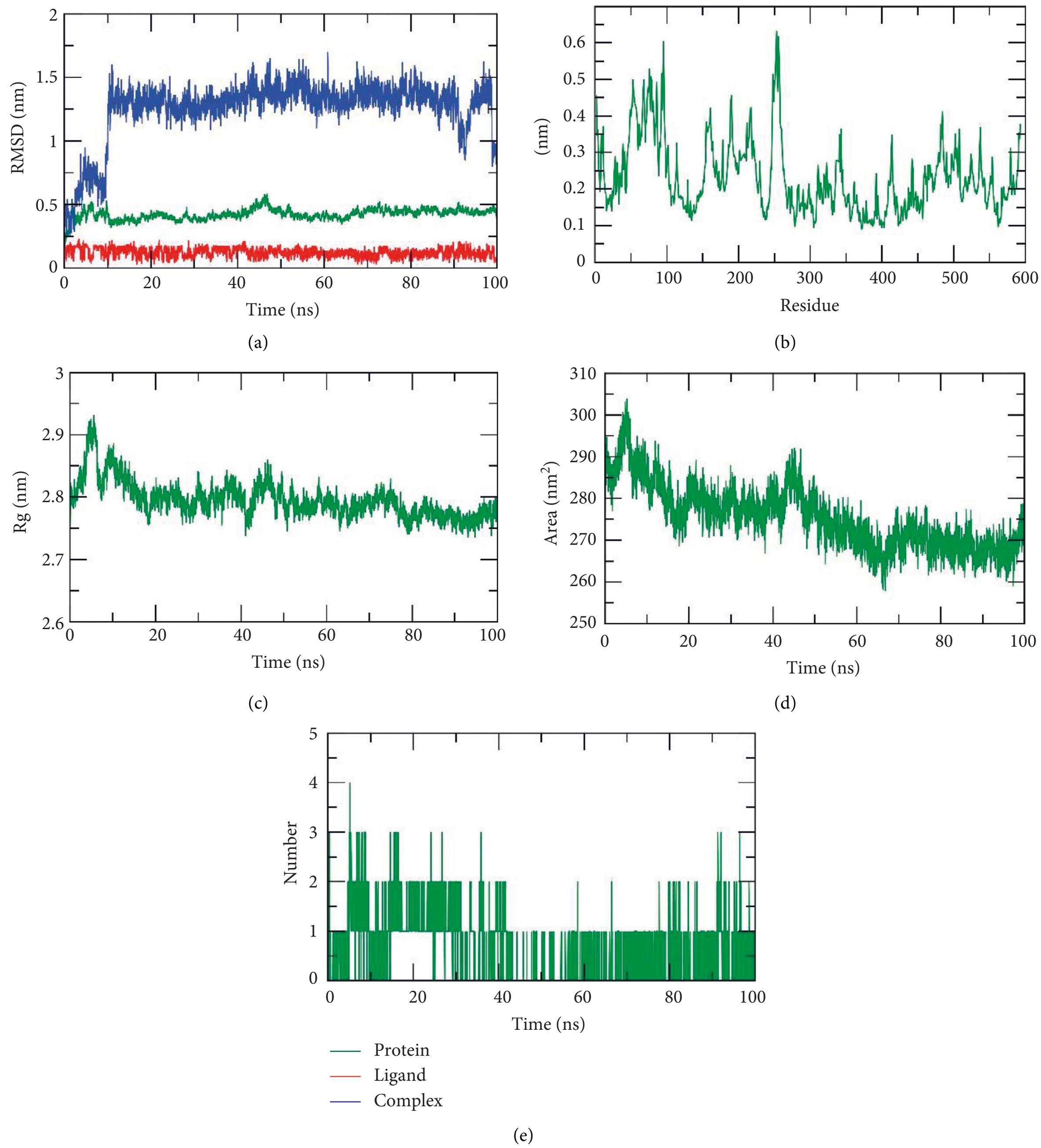

Figure 12: M D simulation results: (a) RMSD values of SARS-CoV-2 helicase, **533,** and SARS-CoV-2 helicase-**533** complex; (b) RMSF for SARS-CoV-2 helicase; (c) R_g of SARS-CoV-2 helicase; (d) SASA of SARS-CoV-2 helicase; and (e) H-bonding between SARS-CoV-2 helicase-**533** complex in the MD run.

helicase-**533** complex during the 100 ns of the MD simulations. The decrease of RMSF values during the MD simulation in 50–100 residue areas (Figure 12(b)) denotes that SARS-CoV-2 residues were more rigid and stabilized after binding to **533**.

Third, the radius of gyration (R_g) is a crucial parameter that is linked to the protein stability according to the change in its volume. R_g is defined as the root mean square distance (RMSD) of a weighted mass group of atoms from their mass center [96, 97]. Thus, the calculation of R_g identifies the dimensions as well as the compactness of the SARS-CoV-2 helicase-**533** complex. The lower degree of fluctuation throughout the simulation period indicates the greater compactness of a system. The R_g of the SARS-CoV-2 helicase-**533** complex was found to be lower than the starting period (Figure 12(c)) displaying compactness and stability.

Fourth, the interaction between protein-ligand complexes and solvents was measured by solvent accessible surface area (SASA) over the simulation period. So, the SASA of the SARS-CoV-2 helicase-**533** complex was calculated to provide the extent of the conformational changes that occurred during binding. Interestingly, SARS-CoV-2

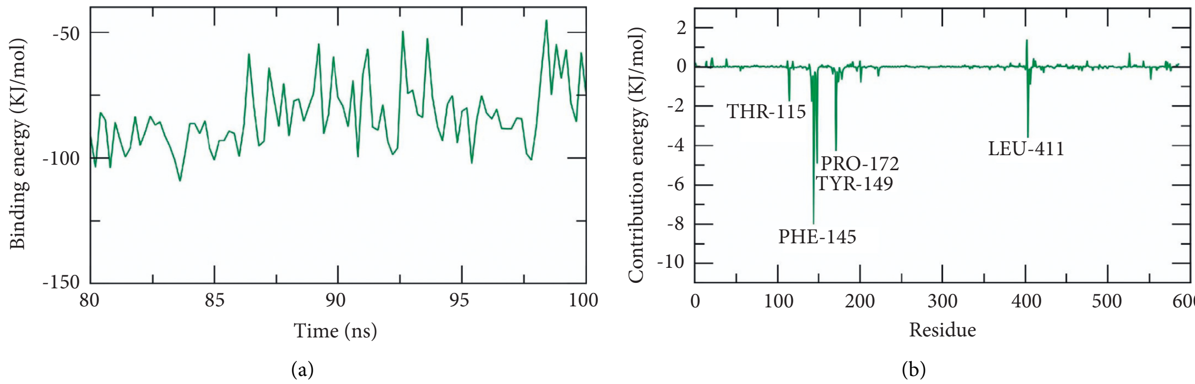

FIGURE 13: MM-PBSA results of SARS-CoV-2 helicase-**1552** complex.

helicase featured a reduction of the surface area showing a relatively lower SASA value than the starting period (Figure 12(d)).

Finally, hydrogen bonding between a SARS-CoV-2 helicase-**533** complex is essential to stabilize the structure. MD simulation studies showed that the highest number of conformations of the SARS-CoV-2 helicase formed up to three hydrogen bonds with **533** (Figure 12(e)).

2.7. Molecular Mechanics Poisson–Boltzmann Surface Area (MM-PBSA). In this experiment, the molecular mechanics Poisson–Boltzmann surface area (MM-PBSA) method was the utilized method to calculate the free binding energy of the SARS-CoV-2 helicase-**533** complex. The MM-PBSA can evaluate the binding between a specific receptor and a ligand through the accurate calculation of the binding free energy of the ligand-protein complex. The MM-PBSA method utilizes both thermodynamic cycle and molecular dynamics (MD) methods to compute the binding free energy. The MM-PBSA calculates the binding free energies according to the following equation: $\Delta G_{\text{bind.}} = G_{\text{comp.}} - (G_{\text{prot.}} + G_{\text{lig.}})$.

$\Delta G_{\text{bind.}}$ refers to the total energy difference that was calculated as the difference between the energy at the bound-state ($G_{\text{comp.}}$) and the sum of energy of both protein ($G_{\text{prot.}}$) and ligand ($G_{\text{lig.}}$) before binding [98]. To compute the biding energy accurately, two main types of energies should be considered: first, the gas-phase interaction energy, which consists of van der Waals and electrostatic interactions; and, second, the solvation energy, which includes both polar and nonpolar components [99].

The MM-PBSA, as a tool to calculate the free binding energies, has several advantages over other methods such as free energy perturbation and thermodynamic integration such as being faster, simpler, and producing consistent results with the experimental [100].

The binding free energy of the SARS-CoV-2 helicase-**533** complex was computed at the last stable 20 ns of the MD production run at a time interval of 100 ps from MD trajectories. The MM/PBSA method was utilized. Also, the MmPbSaStat.py script was employed to calculate the average free binding energy and its standard deviation/error from the output files that were obtained from g_mmpbsa. Compound **533**, (*Z*)-6-(3-hydroxy-4-methoxystyryl)-4-methoxy-2*H*-pyran-2-one, showed a low binding free energy of −83 kJ/mol with the SARS-CoV-2 helicase (Figure 13(a)). The binding energy was stable during all the time of examination indicating the correct binding of the SARS-CoV-2 helicase-**533** complex.

2.7.1. Free Energy Decomposition. The total binding free energy of the SARS-CoV-2 helicase-**533** complex was decomposed to analyze and understand the different components of that obtained binding energy as well as to disclose the contribution of each amino acid residue of the SARS-CoV-2 helicase in the binding with **533**. The total binding free energy was decomposed into per amino acid residue contribution energy. This experiment gives a clearer idea about the essential amino acid residues that have favorable contributions to the binding process. It was found that THR-115, PHE-145, PRO-172, TYR-149, and LEU-411 residues of the protein contributed higher than −2 kJ/mol binding energy and thus they are crucial residues in the binding with **533** (Figure 13(b)).

3. Methods

3.1. Molecular Similarity. Discovery studio 4.0 software was used [101, 102] (see Section 3 in Supplementary data).

3.2. Fingerprints Studies. Discovery studio 4.0 software was used [103, 104] (see Section 3 in Supplementary data).

3.3. Docking Studies. Docking studies were done against the target enzyme using Discovery studio 4.0 software [105, 106] (see Section 3 in Supplementary data).

3.4. ADMET Analysis. Discovery studio 4.0 was used [40, 107] (see Section 3 in Supplementary data).

3.5. Toxicity Studies. Discovery studio 4.0 software was used [108–110] (see Section 3 in Supplementary data).

3.6. Molecular Dynamics Simulation. The system was prepared using the web-based CHARMM-GUI [111–113] utilizing CHARMM36 force field [114] and NAMD 2.13 [115] package. The TIP3P explicit solvation model was used (see supporting data (available here)).

3.7. MM-PBSA Studies. The g_mmpbsa package of GROMACS was utilized to calculate the MM/PBSA (see supporting data (available here)).

4. Conclusion

Twelve of 5956 TCM compounds were suggested to be the potential inhibitors against SARS-CoV-2 helicase (PDB ID: 5RMM). The compounds were selected according to structural similarity and fingerprint studies with **VXG,** the co-crystallized ligand of the target protein. Then, molecular docking studies were carried out. Then, ADMET and toxicity studies were preceded to select the following metabolites: (1*R*,2*S*)-ephedrine (**57**), (1*R*,2*S*)-norephedrine (**59**), 2-(4-(pyrrolidin-1-yl)phenyl)acetic acid (**84**), 1-phenylpropane-1,2-dione (**195**), 2-methoxycinnamic acid (**246**), 2-methoxybenzoic acid (**364**), (*R*)-2-((*R*)-5-oxopyrrolidin-3-yl)-2-phenylacetic acid (**405**), (*Z*)-6-(3-hydroxy-4-methoxystyryl)-4-methoxy-2*H*-pyran-2-one (**533**), 8-chloro-2-(2-phenylethyl)-5,6,7-trihydroxy-5,6,7,8-tetrahydrochromone (**637**), 3-((1*R*,2*S*)-2-(dimethylamino)-1-hydroxypropyl) phenol (**818**), (*R*)-2-ethyl-4-(1-hydroxy-2-(methylamino) ethyl)phenol (**5159**), and (*R*)-2-((1*S*,2*S*,5*S*)-2-benzyl-5-hydroxy-4-methylcyclohex-3-en-1-yl)propane-1,2-diol (**5168**). Among them, compounds **84, 195, 364, 533,** and **637** showed the best docking scores. Interestingly, compound **533**, the one with the highest docking score, bonded favorably to the target protein with low energy and optimum dynamics according to advanced MD simulation studies over 100 ns.

Data Availability

The data that support the findings of this study are included within this article.

Conflicts of Interest

The authors declare that they have no conflicts of interest.

Acknowledgments

This work was financially supported from the Researchers, supporting project no. RSP-2021/103, King Saud University, Riyadh, Saudi Arabia.

Supplementary Materials

Supplementary data contain the detailed methodology and the toxicity reports. (*Supplementary Materials*)

References

[1] WHO, WHO coronavirus (COVID-19) dashboard, https://covid19.who.int/.

[2] A. M. Metwaly, M. M. Ghoneim, I. H. Eissa et al., "Traditional ancient Egyptian medicine: a review," *Saudi Journal of Biological Sciences*, vol. 28, no. 10, pp. 5823–5832, 2021.

[3] A. Metwaly, M. Ghoneim, W. Afifi et al., "Biological evaluation and molecular docking study of metabolites from salvadora persica L. growing in Egypt," *Pharmacognosy Magazine*, vol. 15, no. 61, p. 232, 2019.

[4] L. Liu, S. Luo, M. Yu et al., "Chemical constituents of *Tagetes patula* and their neuroprotecting action," *Natural Product Communications*, vol. 15, no. 11, 2020.

[5] Y.-M. Wang, X.-K. Ran, M. Riaz et al., "Chemical constituents of stems and leaves of *Ttagetes patula* L. and its fingerprint," *Molecules*, vol. 24, no. 21, p. 3911, 2019.

[6] A. M. Metwaly, M. M. Ghoneim, and A. Musa, "Two new antileishmanial diketopiperazine alkaloids from the endophytic fungus Trichosporum sp," *Derpharmachemica*, vol. 7, pp. 322–327, 2015.

[7] A. M. Yassin, N. M. El-Deeb, A. M. Metwaly, G. F. El Fawal, M. M. Radwan, and E. E. Hafez, "Induction of apoptosis in human cancer cells through extrinsic and intrinsic pathways by *Balanites aegyptiaca* furostanol saponins and saponin-coated silver nanoparticles," *Applied Biochemistry and Biotechnology*, vol. 182, no. 4, pp. 1675–1693, 2017.

[8] M. H. Sharaf, G. M. El-Sherbiny, S. A. Moghannem et al., "New combination approaches to combat methicillin-resistant *Staphylococcus aureus* (MRSA)," *Scientific Reports*, vol. 11, pp. 4240–4316, 2021.

[9] A. M. Metwaly, Z. Lianlian, H. Luqi, and D. Deqiang, "Black ginseng and its saponins: preparation, phytochemistry and pharmacological effects," *Molecules*, vol. 24, no. 10, p. 1856, 2019.

[10] A. M. Metwaly, H. A. Kadry, A. A. El-Hela et al., "Nigrosphaerin a new isochromene derivative from the endophytic fungus *Nigrospora sphaerica*," *Phytochemistry Letters*, vol. 7, pp. 1–5, 2014.

[11] A. M. Metwaly, F. R. Fronczek, G. Ma et al., "Antileukemic α-pyrone derivatives from the endophytic fungus *Alternaria phragmospora*," *Tetrahedron Letters*, vol. 55, no. 24, pp. 3478–3481, 2014.

[12] A. M. Metwaly, A. S. Wanas, M. M. Radwan, S. A. Ross, and M. A. ElSohly, "New α-pyrone derivatives from the endophytic fungus *Embellisia* sp," *Medicinal Chemistry Research*, vol. 26, no. 8, pp. 1796–1800, 2017.

[13] A. Zhanzhaxina, Y. Suleimen, A. M. Metwaly et al., "In vitro and in silico cytotoxic and antibacterial activities of a diterpene from *Cousinia alata* Schrenk," *Journal of Chemistry*, vol. 2021, pp. 2021–2111.

[14] V. O. Imieje, A. A. Zaki, A. M. Metwaly et al., *Antileishmanial Derivatives of Humulene from Asteriscus hierochunticus with in silico Tubulin Inhibition Potential*, ACG Publications, Kocaeli, Turkey, 2021.

[15] R. I. Jalmakhanbetova, E. B. Elkaeed, I. H. Eissa, A. M. Metwaly, and Y. M. Suleimen, "Synthesis and molecular docking of some Grossgemin amino derivatives as tubulin inhibitors targeting colchicine binding site," *Journal of Chemistry*, vol. 2021, Article ID 5586515, 10 pages, 2021.

[16] Y. M. Suleimen, A. M. Metwaly, A. E. Mostafa et al., "Isolation, crystal structure, and in silico aromatase inhibition activity of ergosta-5, 22-dien-3β-ol from the fungus

Gyromitra esculenta," *Journal of Chemistry*, vol. 2021, Article ID 5529786, 10 pages, 2021.

[17] L.-J. Xiao and R. Tao, "Traditional Chinese medicine (TCM) therapy," *Advances in Experimental Medicine and Biology*, vol. 2017, no. 1010, pp. 261–280, 2017.

[18] J.-L. Tang, B.-Y. Liu, and K.-W. Ma, "Traditional Chinese medicine," *The Lancet*, vol. 372, no. 9654, pp. 1938–1940, 2008.

[19] X. Han, Y. Yang, A. M. Metwaly, Y. Xue, Y. Shi, and D. Dou, "The Chinese herbal formulae (Yitangkang) exerts an anti-diabetic effect through the regulation of substance metabolism and energy metabolism in type 2 diabetic rats," *Journal of Ethnopharmacology*, vol. 239, Article ID 111942, 2019.

[20] Y. Lao, X. Wang, N. Xu, H. Zhang, and H. Xu, "Application of proteomics to determine the mechanism of action of traditional Chinese medicine remedies," *Journal of Ethnopharmacology*, vol. 155, pp. 1–8, 2014.

[21] J. Xu and A. Hagler, "Chemoinformatics and drug discovery," *Molecules*, vol. 7, no. 8, pp. 566–600, 2002.

[22] T. Engel, "Basic overview of chemoinformatics," *Journal of Chemical Information and Modeling*, vol. 46, no. 6, pp. 2267–2277, 2006.

[23] E. March-Vila, L. Pinzi, N. Sturm et al., "On the integration of in silico drug design methods for drug repurposing," *Frontiers in Pharmacology*, vol. 8, p. 298, 2017.

[24] W. Zhang, J. Pei, and L. Lai, "Computational multitarget drug design," *Journal of Chemical Information and Modeling*, vol. 57, no. 3, pp. 403–412, 2017.

[25] M. I. Youssef, Y. Zhou, I. H. Eissa et al., "Tetradecyl 2, 3-dihydroxybenzoate alleviates oligodendrocyte damage following chronic cerebral hypoperfusion through IGF-1 receptor," *Neurochemistry International*, vol. 138, Article ID 104749, 2020.

[26] F. Zhong, J. Xing, X. Li et al., "Artificial intelligence in drug design," *Science China Life Sciences*, vol. 61, no. 10, pp. 1191–1204, 2018.

[27] M. Hagras, M. A. El Deeb, H. S. A. Elzahabi, E. B. Elkaeed, A. B. M. Mehany, and I. H. Eissa, "Discovery of new quinolines as potent colchicine binding site inhibitors: design, synthesis, docking studies, and anti-proliferative evaluation," *Journal of Enzyme Inhibition and Medicinal Chemistry*, vol. 36, no. 1, pp. 640–658, 2021.

[28] I. H. Eissa, M. A. Dahab, M. K. Ibrahim et al., "Design and discovery of new antiproliferative 1, 2, 4-triazin-3 (2H)-ones as tubulin polymerization inhibitors targeting colchicine binding site," *Bioorganic Chemistry*, vol. 112, Article ID 104965, 2021.

[29] I. H. Eissa, A.-G. A. El-Helby, H. A. Mahdy et al., "Discovery of new quinazolin-4 (3H)-ones as VEGFR-2 inhibitors: design, synthesis, and anti-proliferative evaluation," *Bioorganic Chemistry*, vol. 105, Article ID 104380, 2020.

[30] K. El-Adl, A.-G. A. El-Helby, R. R. Ayyad et al., "Design, synthesis, and anti-proliferative evaluation of new quinazolin-4 (3H)-ones as potential VEGFR-2 inhibitors," *Bioorganic & Medicinal Chemistry*, vol. 29, Article ID 115872, 2021.

[31] A.-G. A. El-Helby, R. R. A. Ayyad, K. El-Adl et al., "Design, molecular docking and synthesis of some novel 4-acetyl-1-substituted-3, 4-dihydroquinoxalin-2 (1 H)-one derivatives for anticonvulsant evaluation as AMPA-receptor antagonists," *Medicinal Chemistry Research*, vol. 25, no. 12, pp. 3030–3046, 2016.

[32] V. Kairys, L. Baranauskiene, M. Kazlauskiene, D. Matulis, and E. Kazlauskas, "Binding affinity in drug design: experimental and computational techniques," *Expert Opinion on Drug Discovery*, vol. 14, no. 8, pp. 755–768, 2019.

[33] T. Al-Warhi, A. M. El Kerdawy, N. Aljaeed et al., "Synthesis, biological evaluation and in silico studies of certain oxindole–indole conjugates as anticancer CDK inhibitors," *Molecules*, vol. 25, no. 9, p. 2031, 2020.

[34] S. A. El-Metwally, M. M. Abou-El-Regal, I. H. Eissa et al., "Discovery of thieno [2, 3-d] pyrimidine-based derivatives as potent VEGFR-2 kinase inhibitors and anti-cancer agents," *Bioorganic Chemistry*, vol. 112, Article ID 104947, 2021.

[35] M. M. Alanazi, I. H. Eissa, N. A. Alsaif et al., "Design, synthesis, docking, ADMET studies, and anticancer evaluation of new 3-methylquinoxaline derivatives as VEGFR-2 inhibitors and apoptosis inducers," *Journal of Enzyme Inhibition and Medicinal Chemistry*, vol. 36, no. 1, pp. 1760–1782, 2021.

[36] M. M. Alanazi, A. Elwan, N. A. Alsaif et al., "Discovery of new 3-methylquinoxalines as potential anti-cancer agents and apoptosis inducers targeting VEGFR-2: design, synthesis, and in silico studies," *Journal of Enzyme Inhibition and Medicinal Chemistry*, vol. 36, no. 1, pp. 1732–1750, 2021.

[37] N. A. Alsaif, M. S. Taghour, M. M. Alanazi et al., "Discovery of new VEGFR-2 inhibitors based on bis ([1, 2, 4] triazolo) [4, 3-a: 3′, 4′-c] quinoxaline derivatives as anticancer agents and apoptosis inducers," *Journal of Enzyme Inhibition and Medicinal Chemistry*, vol. 36, no. 1, pp. 1093–1114, 2021.

[38] N. A. Alsaif, M. A. Dahab, M. M. Alanazi et al., "New quinoxaline derivatives as VEGFR-2 inhibitors with anticancer and apoptotic activity: design, molecular modeling, and synthesis," *Bioorganic Chemistry*, vol. 110, Article ID 104807, 2021.

[39] K. El-Adl, M.-K. Ibrahim, M. S. Alesawy, and I. H. Eissa, "[1, 2, 4] Triazolo [4, 3-c] quinazoline and bis ([1, 2, 4] triazolo) [4, 3-a: 4′, 3′-c] quinazoline derived DNA intercalators: design, synthesis, in silico ADMET profile, molecular docking and anti-proliferative evaluation studies," *Bioorganic & Medicinal Chemistry*, vol. 30, Article ID 115958, 2021.

[40] D. R. Parmar, J. Y. Soni, R. Guduru et al., "Discovery of new anticancer thiourea-azetidine hybrids: design, synthesis, in vitro antiproliferative, SAR, in silico molecular docking against VEGFR-2, ADMET, toxicity, and DFT studies," *Bioorganic Chemistry*, vol. 115, Article ID 105206, 2021.

[41] R. I. Jalmakhanbetova, Y. M. Suleimen, M. Oyama et al., "Isolation and in silico anti-COVID-19 main protease (Mpro) activities of flavonoids and a sesquiterpene lactone from *Artemisia sublessingiana*," *Journal of Chemistry*, vol. 2021, Article ID 5547013, 8 pages, 2021.

[42] A. El-Demerdash, A. M. Metwaly, A. Hassan et al., "Comprehensive virtual screening of the antiviral potentialities of marine polycyclic guanidine alkaloids against SARS-CoV-2 (COVID-19)," *Biomolecules*, vol. 11, no. 3, p. 460, 2021.

[43] M. S. Alesawy, A. E. Abdallah, M. S. Taghour, E. B. Elkaeed, I. H Eissa, and A. M. Metwaly, "In silico studies of some isoflavonoids as potential candidates against COVID-19 targeting human ACE2 (hACE2) and viral main protease (Mpro)," *Molecules*, vol. 26, no. 9, p. 2806, 2021.

[44] I. H. Eissa, M. M. Khalifa, E. B. Elkaeed, E. E. Hafez, A. A. Alsfouk, and A. M. Metwaly, "In silico exploration of potential natural inhibitors against SARS-cov-2 nsp10," *Molecules*, vol. 26, no. 20, p. 6151, 2021.

[45] M. S. Alesawy, E. B. Elkaeed, A. A. Alsfouk, A. M. Metwaly, and I. H. Eissa, "In silico screening of semi-synthesized compounds as potential inhibitors for SARS-CoV-2 papain-like protease: pharmacophoric features, molecular docking, ADMET, toxicity and DFT studies," *Molecules*, vol. 26, no. 21, p. 6593, 2021.
[46] K. A. Ivanov, V. Thiel, J. C. Dobbe, Y. Van Der Meer, E. J. Snijder, and J. Ziebuhr, "Multiple enzymatic activities associated with severe acute respiratory syndrome coronavirus helicase," *Journal of Virology*, vol. 78, no. 11, pp. 5619–5632, 2004.
[47] D. Huttner and I. D. Hickson, "Helicases," in *Brenner's Encyclopedia of Genetics*, S. Maloy and K. Hughes, Eds., , Academic Press, San Diego, CA, USA, 2nd edition, 2013.
[48] P. Ripphausen, B. Nisius, and J. Bajorath, "State-of-the-art in ligand-based virtual screening," *Drug Discovery Today*, vol. 16, no. 9-10, pp. 372–376, 2011.
[49] B. J. Burke, *Developments in Molecular Shape Analysis to Establish Spatial Similarity Among Flexible Molecules*, University of Illinois at Chicago, Health Sciences Center, Chicago, IL, USA, 1993.
[50] P. Willett, "Similarity-based virtual screening using 2D fingerprints," *Drug Discovery Today*, vol. 11, no. 23-24, pp. 1046–1053, 2006.
[51] H. Briem and I. D. Kuntz, "Molecular similarity based on DOCK-generated fingerprints," *Journal of Medicinal Chemistry*, vol. 39, no. 17, pp. 3401–3408, 1996.
[52] P. Willett, "Similarity searching using 2D structural fingerprints," *Methods in Molecular Biology*, vol. 672, pp. 133–158, 2011.
[53] A. M. Hassell, G. An, R. K. Bledsoe et al., "Crystallization of protein–ligand complexes," *Acta Crystallographica Section D Biological Crystallography*, vol. 63, no. 1, pp. 72–79, 2007.
[54] M. A. Spackman and J. J. McKinnon, "Fingerprinting intermolecular interactions in molecular crystals," *CrystEngComm*, vol. 4, no. 66, pp. 378–392, 2002.
[55] H. Chu, Q.-x. He, J. Wang, Y. Hu, Y.-q. Wang, and Z.-h. Lin, "In silico design of novel benzohydroxamate-based compounds as inhibitors of histone deacetylase 6 based on 3D-QSAR, molecular docking, and molecular dynamics simulations," *New Journal of Chemistry*, vol. 44, no. 48, pp. 21201–21210, 2020.
[56] C. Ieritano, J. L. Campbell, and W. S. Hopkins, "Predicting differential ion mobility behaviour in silico using machine learning," *Analyst*, vol. 146, no. 15, pp. 4737–4743, 2021.
[57] M. Taha, N. H. Ismail, M. Ali et al., "Molecular hybridization conceded exceptionally potent quinolinyl-oxadiazole hybrids through phenyl linked thiosemicarbazide antileishmanial scaffolds: in silico validation and SAR studies," *Bioorganic Chemistry*, vol. 71, pp. 192–200, 2017.
[58] K. Heikamp and J. R. Bajorath, "How do 2D fingerprints detect structurally diverse active compounds? Revealing compound subset-specific fingerprint features through systematic selection," *Journal of Chemical Information and Modeling*, vol. 51, no. 9, pp. 2254–2265, 2011.
[59] F. A. D. M. Opo, M. M. Rahman, F. Ahammad, I. Ahmed, M. A. Bhuiyan, and A. M. Asiri, "Structure based pharmacophore modeling, virtual screening, molecular docking and ADMET approaches for identification of natural anticancer agents targeting XIAP protein," *Scientific Reports*, vol. 11, pp. 4049–4117, 2021.
[60] J. Duan, M. Sastry, S. Dixon, J. Lowrie, and W. Sherman, "Analysis and comparison of 2D fingerprints: insights into database screening performance using eight fingerprint methods," *Journal of Cheminformatics*, vol. 3, no. S1, pp. 157–170, 2011.
[61] M. Sastry, J. F. Lowrie, S. L. Dixon, and W. Sherman, "Large-scale systematic analysis of 2D fingerprint methods and parameters to improve virtual screening enrichments," *Journal of Chemical Information and Modeling*, vol. 50, no. 5, pp. 771–784, 2010.
[62] T. Kogej, O. Engkvist, N. Blomberg, and S. Muresan, "Multifingerprint based similarity searches for targeted class compound selection," *Journal of Chemical Information and Modeling*, vol. 46, no. 3, pp. 1201–1213, 2006.
[63] I. Muegge and P. Mukherjee, "An overview of molecular fingerprint similarity search in virtual screening," *Expert Opinion on Drug Discovery*, vol. 11, no. 2, pp. 137–148, 2016.
[64] G. Maggiora, M. Vogt, D. Stumpfe, and J. Bajorath, "Molecular similarity in medicinal chemistry: miniperspective," *Journal of Medicinal Chemistry*, vol. 57, no. 8, pp. 3186–3204, 2014.
[65] M. Turchi, Q. Cai, and G. Lian, "An evaluation of in-silico methods for predicting solute partition in multiphase complex fluids–a case study of octanol/water partition coefficient," *Chemical Engineering Science*, vol. 197, pp. 150–158, 2019.
[66] K. M. Sullivan, S. J. Enoch, J. Ezendam, K. Sewald, E. L. Roggen, and S. Cochrane, "An adverse outcome pathway for sensitization of the respiratory tract by low-molecular-weight chemicals: building evidence to support the utility of in vitro and in silico methods in a regulatory context," *Applied In Vitro Toxicology*, vol. 3, pp. 213–226, 2017.
[67] T. Altamash, A. Amhamed, S. Aparicio, and M. Atilhan, "Effect of hydrogen bond donors and acceptors on CO_2 absorption by deep eutectic solvents," *Processes*, vol. 8, no. 12, p. 1533, 2020.
[68] Y. Wan, Y. Tian, W. Wang, S. Gu, X. Ju, and G. Liu, "In silico studies of diarylpyridine derivatives as novel HIV-1 NNRTIs using docking-based 3D-QSAR, molecular dynamics, and pharmacophore modeling approaches," *RSC Advances*, vol. 8, no. 71, pp. 40529–40543, 2018.
[69] A. Escamilla-Gutiérrez, R. M. Ribas-Aparicio, M. G. Córdova-Espinoza, and J. A. Castelán-Vega, "In silico strategies for modeling RNA aptamers and predicting binding sites of their molecular targets," *Nucleosides, Nucleotides & Nucleic Acids*, vol. 40, no. 8, pp. 798–807, 2021.
[70] A. C. Kaushik, A. Kumar, S. Bharadwaj, R. Chaudhary, and S. Sahi, "Ligand-based approach for in-silico drug designing," in *Bioinformatics Techniques for Drug Discovery*, pp. 11–19, Springer, Berlin, Germany, 2018.
[71] A. N. Jain, "Morphological similarity: a 3D molecular similarity method correlated with protein-ligand recognition," *Journal of Computer-Aided Molecular Design*, vol. 14, no. 2, pp. 199–213, 2000.
[72] H. Zhang, J.-X. Ren, J.-X. Ma, and L. Ding, "Development of an in silico prediction model for chemical-induced urinary tract toxicity by using naïve Bayes classifier," *Molecular Diversity*, vol. 23, no. 2, pp. 381–392, 2019.
[73] L. L. Ferreira and A. D. Andricopulo, "ADMET modeling approaches in drug discovery," *Drug Discovery Today*, vol. 24, no. 5, pp. 1157–1165, 2019.
[74] U. Norinder and C. A. Bergström, "Prediction of ADMET properties," *ChemMedChem*, vol. 1, no. 9, pp. 920–937, 2006.
[75] J. C. Dearden, "In silico prediction of drug toxicity," *Journal of Computer-Aided Molecular Design*, vol. 17, no. 2-4, pp. 119–127, 2003.

[76] G. Idakwo, J. Luttrell, M. Chen et al., "A review on machine learning methods for in silico toxicity prediction," *Journal of Environmental Science and Health, Part C*, vol. 36, no. 4, pp. 169–191, 2018.

[77] N. L. Kruhlak, R. D. Benz, H. Zhou, and T. J. Colatsky, "(Q) SAR modeling and safety assessment in regulatory review," *Clinical Pharmacology & Therapeutics*, vol. 91, no. 3, pp. 529–534, 2012.

[78] X. Xia, E. G. Maliski, P. Gallant, and D. Rogers, "Classification of kinase inhibitors using a Bayesian model," *Journal of Medicinal Chemistry*, vol. 47, no. 18, pp. 4463–4470, 2004.

[79] BIOVIA. QSAR, ADMET and Predictive Toxicology, 2020, https://www.3dsbiovia.com/products/collaborative-science/biovia-discovery-studio/qsar-admet-and-predictive-toxicology.html.

[80] R. Venkatapathy, N. C. Y. Wang, T. M. Martin, P. F. Harten, and D. Young, "Structure–activity relationships for carcinogenic potential," *General, Applied and Systems Toxicology*, Wiley, Hoboken, NJ, USA, 2009.

[81] G. Goodrnan and R. Wilson, "Comparison of the dependence of the TD50 on maximum tolerated dose for mutagens and nonmutagens," *Risk Analysis*, vol. 12, no. 4, pp. 525–533, 1992.

[82] N. R. Council, "Correlation between carcinogenic potency and the maximum tolerated dose: implications for risk assessment," in *Issues in Risk Assessment*National Academies Press, Washington, DC, USA, 1993.

[83] R. Gonella Diaza, S. Manganelli, A. Esposito, A. Roncaglioni, A. Manganaro, and E. Benfenati, "Comparison of in silico tools for evaluating rat oral acute toxicity," *SAR and QSAR in Environmental Research*, vol. 26, pp. 1–27, 2015.

[84] F. Pizzo and E. Benfenati, "In silico models for repeated-dose toxicity (RDT): prediction of the no observed adverse effect level (NOAEL) and lowest observed adverse effect level (LOAEL) for drugs," *Silico Methods for Predicting Drug Toxicity*, pp. 163–176, Springer, Berlin, Germany, 2016.

[85] R. Venkatapathy, C. J. Moudgal, and R. M. Bruce, "Assessment of the oral rat chronic lowest observed adverse effect level model in TOPKAT, a QSAR software package for toxicity prediction," *Journal of Chemical Information and Computer Sciences*, vol. 44, no. 5, pp. 1623–1629, 2004.

[86] K. R. Wilhelmus, "The Draize eye test," *Survey of Ophthalmology*, vol. 45, no. 6, pp. 493–515, 2001.

[87] S. F. Sousa, P. A. Fernandes, and M. J. Ramos, "Protein–ligand docking: current status and future challenges," *Proteins: Structure, Function, and Bioinformatics*, vol. 65, no. 1, pp. 15–26, 2006.

[88] S. A. Hollingsworth and R. O. Dror, "Molecular dynamics simulation for all," *Neuron*, vol. 99, no. 6, pp. 1129–1143, 2018.

[89] X. Liu, D. Shi, S. Zhou, H. Liu, H. Liu, and X. Yao, "Molecular dynamics simulations and novel drug discovery," *Expert Opinion on Drug Discovery*, vol. 13, no. 1, pp. 23–37, 2018.

[90] T. Hansson, C. Oostenbrink, and W. van Gunsteren, "Molecular dynamics simulations," *Current Opinion in Structural Biology*, vol. 12, no. 2, pp. 190–196, 2002.

[91] J. A. McCammon, B. R. Gelin, and M. Karplus, "Dynamics of folded proteins," *Nature*, vol. 267, no. 5612, pp. 585–590, 1977.

[92] R. Salomon-Ferrer, A. W. Gotz, D. Poole, S. Le Grand, and R. C. Walker, "Routine microsecond molecular dynamics simulations with AMBER on GPUs. 2. Explicit solvent particle mesh Ewald," *Journal of Chemical Theory and Computation*, vol. 9, pp. 3878–3888, 2013.

[93] J. D. Durrant and J. A. McCammon, "Molecular dynamics simulations and drug discovery," *BMC Biology*, vol. 9, pp. 71–79, 2011.

[94] S. Kalyaanamoorthy and Y.-P. P. Chen, "Modelling and enhanced molecular dynamics to steer structure-based drug discovery," *Progress in Biophysics and Molecular Biology*, vol. 114, no. 3, pp. 123–136, 2014.

[95] A. Kuzmanic and B. Zagrovic, "Determination of ensemble-average pairwise root mean-square deviation from experimental B-factors," *Biophysical Journal*, vol. 98, no. 5, pp. 861–871, 2010.

[96] P. Liu, J. Lu, H. Yu, N. Ren, F. E. Lockwood, and Q. J. Wang, "Lubricant shear thinning behavior correlated with variation of radius of gyration via molecular dynamics simulations," *The Journal of chemical physics*, vol. 147, no. 8, Article ID 084904, 2017.

[97] K. M. Kumar, A. Anbarasu, and S. Ramaiah, "Molecular docking and molecular dynamics studies on β-lactamases and penicillin binding proteins," *Molecular BioSystems*, vol. 10, no. 4, pp. 891–900, 2014.

[98] N. Homeyer and H. Gohlke, "Free energy calculations by the molecular mechanics Poisson−Boltzmann surface area method," *Molecular Informatics*, vol. 31, no. 2, pp. 114–122, 2012.

[99] H. Sun, Y. Li, M. Shen et al., "Assessing the performance of MM/PBSA and MM/GBSA methods. 5. Improved docking performance using high solute dielectric constant MM/GBSA and MM/PBSA rescoring," *Physical Chemistry Chemical Physics*, vol. 16, no. 40, pp. 22035–22045, 2014.

[100] J. Ren, X. Yuan, J. Li et al., "Assessing the performance of the g_mmpbsa tools to simulate the inhibition of oseltamivir to influenza virus neuraminidase by molecular mechanics Poisson–Boltzmann surface area methods," *Journal of the Chinese Chemical Society*, vol. 67, no. 1, pp. 46–53, 2020.

[101] I. H. Eissa, M. S. Alesawy, A. M. Saleh, E. B. Elkaeed, B. A. Alsfouk, and A.-A. M. M. El-Attar, "Silico determination of the most promising SARS-CoV-2 nsp16-nsp10 $2'$-o-methyltransferase complex inhibitors among 3009 FDA approved drugs," *Molecules*, vol. 27, p. 2287, 2022.

[102] Y. M. Suleimen, R. A. Jose, R. N. Suleimen et al., "Jusanin, a new flavonoid from *Artemisia commutata* with an in silico inhibitory potential against the SARS-CoV-2 main protease," *Molecules*, vol. 27, no. 5, p. 1636, 2022.

[103] Y. M. Suleimen, R. A. Jose, R. N. Suleimen et al., "Isolation and in silico SARS-CoV-2 main protease inhibition potential of jusan coumarin, a new dicoumarin from *Artemisia glauca*," *Molecules*, vol. 27, no. 7, p. 2281, 2022.

[104] E. B. Elkaeed, H. Elkady, A. Belal et al., "Multi-phase in silico discovery of potential SARS-CoV-2 RNA-dependent RNA polymerase inhibitors among 3009 clinical and FDA-approved related drugs," *Processes*, vol. 10, no. 3, p. 530, 2022.

[105] R. P. D. Bank, 2020, https://www.rcsb.org/structure/4OW0.

[106] Y. M. Suleimen, R. A. Jose, R. N. Suleimen et al., "Isolation and in silico anti-SARS-CoV-2 papain-like protease potentialities of two rare 2-phenoxychromone derivatives from Artemisia spp," *Molecules*, vol. 27, no. 4, p. 1216, 2022.

[107] S. O. Mohammed, S. H. E. El Ashry, A. Khalid et al., "Expression, purification, and comparative inhibition of *Helicobacter pylori* urease by regio-selectively alkylated benzimidazole 2-thione derivatives," *Molecules*, vol. 27, no. 3, p. 865, 2022.

[108] R. G. Yousef, H. M. Sakr, I. H. Eissa et al., "New quinoxaline-2 (1H)-ones as potential VEGFR-2 inhibitors: design, synthesis, molecular docking, ADMET profile and anti-

proliferative evaluations," *New Journal of Chemistry*, vol. 45, no. 36, pp. 16949–16964, 2021.

[109] H. H. Amer, S. H. Alotaibi, A. H. Trawneh, A. M. Metwaly, and I. H. Eissa, "Anticancer activity, spectroscopic and molecular docking of some new synthesized sugar hydrazones, Arylidene and α-Aminophosphonate derivatives," *Arabian Journal of Chemistry*, vol. 14, no. 10, Article ID 103348, 2021.

[110] M. S. Alesawy, A. A. Al-Karmalawy, E. B. Elkaeed et al., "Design and discovery of new 1, 2, 4-triazolo [4, 3-c] quinazolines as potential DNA intercalators and topoisomerase II inhibitors," *Archiv der Pharmazie*, vol. 354, no. 3, Article ID 2000237, 2021.

[111] S. Jo, T. Kim, V. G. Iyer, and W. Im, "CHARMM-GUI: a web-based graphical user interface for CHARMM," *Journal of Computational Chemistry*, vol. 29, no. 11, pp. 1859–1865, 2008.

[112] B. R. Brooks, C. L. Brooks III, A. D. Mackerell Jr. et al., "CHARMM: the biomolecular simulation program," *Journal of Computational Chemistry*, vol. 30, no. 10, pp. 1545–1614, 2009.

[113] J. Lee, X. Cheng, J. M. Swails et al., "CHARMM-GUI input generator for NAMD, GROMACS, AMBER, OpenMM, and CHARMM/OpenMM simulations using the CHARMM36 additive force field," *Journal of Chemical Theory and Computation*, vol. 12, no. 1, pp. 405–413, 2016.

[114] R. B. Best, X. Zhu, J. Shim et al., "Optimization of the additive CHARMM all-atom protein force field targeting improved sampling of the backbone ϕ, ψ and side-chain χ_1 and χ_2 dihedral angles," *Journal of Chemical Theory and Computation*, vol. 8, no. 9, pp. 3257–3273, 2012.

[115] J. C. Phillips, R. Braun, W. Wang et al., "Scalable molecular dynamics with NAMD," *Journal of Computational Chemistry*, vol. 26, no. 16, pp. 1781–1802, 2005.